The Astrophysical Journal, 707:1141–1159, 2009 December 20 doi:10.1088/0004-637X/707/2/1141

EFFECTS OF THE NON-EQUIPARTITION OF ELECTRONS AND IONS IN THE OUTSKIRTS OF RELAXED GALAXY CLUSTERS

Ka-Wah Wong and Craig L. Sarazin
Department of Astronomy, University of Virginia, P.O. Box 400325, Charlottesville, VA 22904-4325, USA;
kwwong@virginia.edu, sarazin@virginia.edu
Received 2009 August 20; accepted 2009 October 30; published 2009 December 2

ABSTRACT

We have studied the effects of electron–ion non-equipartition in the outer regions of relaxed clusters for a wide range of masses in the ΛCDM cosmology using one-dimensional hydrodynamic simulations. The effects of the non-adiabatic electron heating efficiency, β, on the degree of non-equipartition are also studied. Using the gas fraction $f_{\rm gas} = 0.17$ (which is the upper limit for a cluster), we give a conservative lower limit of the non-equipartition effect on clusters. We have shown that for a cluster with a mass of $M_{\rm vir} \sim 1.2 \times 10^{15}\, M_\odot$, electron and ion temperatures differ by less than a percent within the virial radius $R_{\rm vir}$. The difference is ≈20% for a non-adiabatic electron heating efficiency of $\beta \sim 1/1800$ to 0.5 at $\sim 1.4 R_{\rm vir}$. Beyond that radius, the non-equipartition effect depends rather strongly on β, and such a strong dependence at the shock radius can be used to distinguish shock heating models or constrain the shock heating efficiency of electrons. With our simulations, we have also studied systematically the signatures of non-equipartition on X-ray and Sunyaev–Zel'dovich (SZ) observables. We have calculated the effect of non-equipartition on the projected temperature and X-ray surface brightness profiles using the MEKAL emission model. We found that the effect on the projected temperature profiles is larger than that on the deprojected (or physical) temperature profiles. The non-equipartition effect can introduce a ∼10% bias in the projected temperature at $R_{\rm vir}$ for a wide range of β. We also found that the effect of non-equipartition on the projected temperature profiles can be enhanced by increasing metallicity. In the low-energy band $\lesssim$1 keV, the non-equipartition model surface brightness can be higher than that of the equipartition model in the cluster outer regions. Future X-ray observations extending to $\sim R_{\rm vir}$ or even close to the shock radius should be able to detect these non-equipartition signatures. For a given cluster, the difference between the SZ temperature decrements for the equipartition and the non-equipartition models, $\delta\Delta T_{\rm SZE}$, is larger at a higher redshift. For the most massive clusters at $z \approx 2$, the differences can be $\delta\Delta T_{\rm SZE} \approx 4$–5 μK near the shock radius. We also found that for our model in the ΛCDM universe, the integrated SZ bias, $Y_{\rm non\text{-}eq}/Y_{\rm eq}$, evolves slightly (at a percentage level) with redshift, which is in contrast to the self-similar model in the Einstein–de Sitter universe. This may introduce biases in cosmological studies using the $f_{\rm gas}$ technique. We discussed briefly whether the equipartition and non-equipartition models near the shock region can be distinguished by future radio observations with, for example, the Atacama Large Millimeter Array.

Key words: cosmic microwave background – galaxies: clusters: general – hydrodynamics – intergalactic medium – shock waves – X-rays: galaxies: clusters

Online-only material: color figures

1. INTRODUCTION

Observational and theoretical studies have shown that the study of the intracluster medium (ICM) can be used as a test of plasma physics under extreme environments that cannot be achieved in terrestrial laboratories, as well as an important cosmological probe. If we assume the matter content of clusters is a fair sample of the universe, the baryon fraction of clusters can be used as an estimator of the average value for the universe, with proper correction for the baryons contained in the stellar component and for a small amount of baryonic matter expelled from clusters during the formation process. Recent work from Allen et al. (2008) has shown that the combined results of the baryon fraction from X-ray observation with the cosmic microwave background (CMB) data can give powerful constraints on cosmological parameters, such as the equation of state of the dark energy.

However, the study of cosmology using clusters of galaxies relies heavily on the understanding of cluster physics. For precision cosmology, systematic uncertainties at even the percent level are significant. For example, in current studies, the baryon fraction within clusters is assumed to be independent of redshift and the mass of clusters. It would be important to see if these assumptions are justified; if not, it is important to study the dependence of the baryon fraction on cluster properties and redshift. Even if the dependence on redshift is weak, the correction factor for the baryon content within clusters compared to the average value in the universe could affect the constraints on cosmological parameters.

Studying cluster outskirts ($\gtrsim R_{200}$[1]) is very important because the boundary conditions of the cluster outskirts constrain the global properties of a cluster (e.g., Tozzi et al. 2000). Also, the outer envelopes of clusters have been thought to be less subject to some additional physics including active galactic nucleus (AGN) feedback, and that the outer regions of clusters may provide better cosmological probes. Currently, there are very few observations of the properties of the ICM in the outer parts of clusters. Thus, most of our understanding of these regions is still based on numerical hydrodynamic simulations which assume the hot plasma is a fluid. In these simulations, the clusters

[1] R_Δ is the radius within which the mean total mass density of the cluster is Δ times the critical density. The virial radius $R_{\rm vir}$ is defined as a radius within which the cluster is virialized. For the Einstein–de Sitter universe, $R_{\rm vir} \approx R_{178}$, while for the standard ΛCDM universe, $R_{\rm vir} \approx R_{95}$.

are formed from mergers and accretion of dark matter and baryonic gas in overdense regions. A variety of shocks with different geometries along the large-scale structure (LSS) filaments and transverse to them near and beyond the virial radius are unambiguous predictions of the cosmological hydrodynamic simulations. Unfortunately, the lack of observational information on the clusters outskirts prevents us from understanding the accretion shock region, and hence the input physics for the numerical simulations is called into question. For example, the thermodynamic state of the shocked gas, as well as the shock position, depends on the pre-shock gas temperature; the shock will be weaker if the infalling gas is pre-heated (Tozzi et al. 2000). Even worse, recently it was noted that the non-fluid properties may be important in regions near the virial radius, where the Coulomb collisional mean free path is comparable to the cluster size of a few Mpc (Loeb 2007). The Coulomb collisional timescale can also be of the order of the age of the cluster. This suggests that a full kinetic gas theory is needed instead of the fluid approximation when studying the gas properties near the edge of the cluster. Direct consequences include non-equipartition between electrons and ions (Fox & Loeb 1997; Ettori & Fabian 1998), element sedimentation (Chuzhoy & Loeb 2004), and suprathermal evaporation of hot gas from the clusters (Loeb 2007; see also Medvedev 2007). Some of these effects can lead to a bias in baryon fraction measurements, and hence cosmological studies.

Recently, progress has been made in the study the baryon content of the outer regions of clusters through the X-ray observations together with the Sunyaev–Zel'dovich (SZ) effect on the CMB by the hot electrons in the ICM out to $\sim R_{200}$ (Afshordi et al. 2007). A 3σ result from the *WMAP* three-year data suggests that $35\% \pm 8\%$ of the thermal energy in ICM are missing, indicating that the baryons in clusters may be missing even accounting for those locked in stars. The result is also supported by independent measurements from other X-ray and SZ observations (Ettori 2003; LaRoque et al. 2006; Vikhlinin et al. 2006; Evrard et al. 2008). Using the X-ray observations together with numerical simulations, Evrard et al. (2008) reported that as much as 50% of the thermal energy can be missing in the ICM. Although Giodini et al. (2009) reported that the total baryon fraction within a smaller radius of R_{500} of massive clusters are consistent to the cosmic value within 1σ when all the X-ray hot gas, stellar mass in galaxies, gas depletion during cluster formation, and intracluster light from stars are taken into account, if the missing baryons measured in the outer region ($\lesssim R_{200}$) is really significant, this may indicate either a yet-unknown baryonic component, or some new astrophysical processes in the ICM which is driving out the gas from the clusters. While there is no evidence for any undetected baryonic component, Afshordi et al. (2007) pointed out that the missing of hot baryons can either be explained by the thermal diffusion or the evaporation of baryons out of the virial radius of clusters. Another possibility is that electron temperature is lower than that of the equipartition value (Wong et al. 2008).

Given the advancements in the X-ray and SZ observations of the cluster outer regions (Afshordi et al. 2007; Reiprich et al. 2009; Bautz et al. 2009; George et al. 2009), as well as the growing evidence of missing thermal energy in the ICM and the possible negative implications for cosmological tests, a more detailed study of the kinetic processes in cluster envelopes is necessary. While magnetic fields may affect some of the kinetic effects of transport processes such as thermal conduction, the magnetic effects on non-equipartition should not be important since the physics is local. Moreover, it is known that various astrophysical shocks in magnetized environment lead to non-equipartition (Ghavamian et al. 2007; Hull et al. 2001).

The collisionless accretion shock at the outer boundary of a cluster should primarily heat the ions since they carry most of the kinetic energy of the infalling gas. Assuming that cluster accretion shocks are similar to those in supernova remnants, the electron temperature, T_e, immediately behind the shock would be lower than the ion temperature, T_i. The equilibration between electrons and ions would then proceed by Coulomb collisions. Near the virial radius, due to the low density, the Coulomb collisional timescale can be comparable to the age of the cluster, and the electrons and ions may not achieve equipartition in these regions (Fox & Loeb 1997). Since X-ray and SZ observations measure the properties of the electrons in the ICM, the net effect is to underestimate the total thermal energy content within clusters. This might account for some or all of the missing thermal energy in the ICM derived by the X-ray and SZ observations. As mentioned above, non-equipartition of ions and electrons is observed in various astrophysical shocks. Most supernova remnants with high Mach numbers comparable to cluster accretion shocks have electron temperatures which are lower than the ion temperatures (Ghavamian et al. 2007); in situ measurements from satellites show the same feature in the Earth's bow shock (Hull et al. 2001). On the other hand, X-ray observations of the merger shock in the Bullet Cluster indicate that the equilibration time may be shorter than that expected from Coulomb collisions alone (Markevitch & Vikhlinin 2007). However, this merger shock has a Mach number of a few. From both supernova remnant measurements and a physical model, Ghavamian et al. (2007) have shown that electron heating efficiency within a shock front (usually tens of the gyroradius) is inversely proportional to the Mach number squared. If the results can also be applied to the ICM, the low Mach number merger shocks would be immediately heated to $T_e/T_i \sim 1$, while cosmological accretion shocks with much higher Mach numbers would only be heated to $T_e/T_i \ll 1$ by collisionless processes. After the electrons and ions pass through the thin shock front, they will likely be equilibrated by Coulomb collisions alone (Bykov et al. 2008a, 2008b).

The non-equipartition in cluster of galaxies has been previously studied by Fox & Loeb (1997) and Ettori & Fabian (1998) in semianalytic models. They have shown that the temperature difference can be significant in the outer one-third of the shock radius of a cluster. One- or three-dimensional simulations for some individual clusters have also been studied (Chieze et al. 1998; Takizawa 1999; Rudd & Nagai 2009). While these simulations use different cluster or cosmological models, a general agreement is that the effect of non-equipartition is important if shock heating efficient of electrons is low ($\ll 1$) and the equilibration afterward is due to Coulomb collisions alone.

In this paper, we study systematically the effects of non-equipartition on X-ray and SZ observables in outer regions of relaxed galaxy clusters, which is particularly important for cosmological studies. We carry out one-dimensional hydrodynamic simulations with realistic Navarro–Frenk–White (NFW) model under the concordance ΛCDM cosmological background to provide a sample of clusters (groups) with different masses (10^{13}–$10^{16}\,M_\odot$) at different redshifts ($z = 0$–2). Even though we are studying the kinetic non-fluid properties in the cluster outer regions, the hydrodynamic treatment in modeling the cluster dynamical properties is reasonable and is justified as follows. Even dynamically unimportant magnetic fields should be able to reduce significantly the diffusion mean free path

perpendicular to the magnetic field (Sarazin 1986; Borgani & Kravtsov 2009). The suppression of diffusion in a plasma depends on the topology of magnetic fields. For uniform magnetic fields, only diffusion perpendicular to the local magnetic field is suppressed, and along the field, particles move freely; their mean free path along a field line is still determined by Coulomb collisions. On large scales, diffusion is suppressed in bulk only if the magnetic fields are random and highly tangled on small scales. To include anisotropic diffusion in the calculation would be difficult since the magnetic field structure is not known well enough. However, there is some evidence from large-scale magnetohydrodynamic simulations that magnetic fields in galaxy clusters are chaotic with correlation and reversal length scales of ∼50 and ∼100 kpc, respectively (Dolag et al. 2002). Hence, we simply assume that diffusion is suppressed. We also assume that electrons and ions are equilibrated locally on a long Coulomb collisional timescale, and assume that equilibration via plasma instabilities (Schekochihin et al. 2005, 2008) does not occur except at the shocks (see Section 3). Previous studies show that the dynamical properties of cluster outer regions in one-dimensional simulations successfully reproduce those simulated in three-dimensional calculations (Navarro et al. 1995; Ryu & Kang 1997). The advantages of the one-dimensional simulations for our problem are presented in Section 2. We emphasize the signatures of non-equipartition on X-ray and SZ observations in our studies. We also study the effect of electron shock heating efficiency on the degree of non-equipartition. Thus, observations of electron–ion equilibration may give constraints to the electron heating efficiency, and hence the electron heating mechanism. The wider parameter space compared to previous work explored in this paper allows us to study the impact of non-equipartition effects on cosmological studies in a future paper.

The paper is organized as follows. In Section 2, we describe the set up of our hydrodynamic models. The detailed implementations of the shock heating and the Coulomb equilibration process for our simulations are presented in Section 3. The ability of our simulations to reproduce analytic test models relevant to our studies is discussed in Section 4. We present the simulated dynamics of our realistic NFW cluster models in the standard ΛCDM cosmology in Section 5. These cluster models are used to study the non-equipartition effects presented in the paper. We define the X-ray and SZ observables for our models to be studied, and also present the results for these observables in Section 6. We discuss and conclude our work in Section 7. Unless otherwise specified, we assume the Hubble constant $H_0 = 71.9h_{71.9}$ km s^{-1} Mpc^{-1} with $h_{71.9} = 1$, the total matter density parameter $\Omega_{M,0} = 0.258$, the dark energy density parameter $\Omega_\Lambda = 0.742$, and the gas fraction $f_{\rm gas} = \Omega_b/\Omega_M = 0.17$, where Ω_b is the baryon density parameter, for the realistic NFW model in the standard ΛCDM cosmology,[2] and a hydrogen mass fraction $X = 76\%$ for the ICM throughout the paper.

2. HYDRODYNAMIC MODEL

LSS cosmological simulations predict that clusters do not evolve in isolation. During the linear phase of structure growth, they can be influenced by tidal forces; while during the nonlinear growth phase, they can grow by accreting a significant number of smaller clusters or merging with clusters with similar sizes. However, here we are interested in studying the structure of accretion shocks in clusters, which can be observed most easily in relaxed clusters which have not undergone a recent major merger. Cosmological studies using the gas fraction in clusters are restricted to clusters with the highest degree of dynamical relaxation to minimize systematic scatter in the determination of cosmological parameters (Allen et al. 2008); thus, relaxed clusters are of particular interest. Moreover, based on a set of high resolution *N*-body simulations, it has been found that the mass accretion history of a dark matter halo in general consists of two distinct phases: an early fast phase and a late slow phase (Wechsler et al. 2002; Zhao et al. 2003a, 2003b; Li et al. 2007). The fast accretion phase is dominated by major mergers, while the slow accretion phase is dominated by smooth accretion of background materials and many minor mergers. We are most interested in studying the non-equipartition of electrons and ions in the outer regions of clusters, where materials should be continuously accreting and the morphology is roughly spherical symmetric. Therefore, in our models, we simply consider cluster growth by smooth accretion of materials from the background cosmology. In particular, we assume clusters are spherically symmetric and employ one-dimensional hydrodynamic simulations. It has been shown that one-dimensional calculations reproduce the density and temperature profiles of three-dimensional simulations of clusters in the outer regions (Navarro et al. 1995; Ryu & Kang 1997), where we are most interested. The assumption of spherical symmetry should be sufficient for us to gain insight into the astrophysical effects of non-equipartition on X-ray and SZ observations, as well as the impact on cosmological studies (Wong et al. 2008). Moreover, one-dimensional simulations also allow us to better resolve shocked regions and to isolate the individual physical processes we are interested in, so that non-fluid properties there can be studied in detail. This is difficult to achieve in three-dimensional simulations. Even though three-dimensional simulations have shown that accretion through filaments is a general feature in related clusters, these simulations also show that, other than the filament regions, material is accreted spherically and the morphology in the outer skirts of a clusters are roughly spherical symmetric (Molnar et al. 2009). A very recent three-dimensional study has already shown that the signature of non-equipartition for a relaxed cluster is roughly spherical symmetric as well (model CL104 in Rudd & Nagai 2009).

2.1. Simulation Code

We employed the PLUTO code (Mignone et al. 2007) to solve the one-dimensional Newtonian hydrodynamic equations in spherical coordinates for our problem. This code provides a multi-physics, multi-algorithm modular environment which allows new physics to be included and new modules to be developed easily. The code does not include self-gravity or an *N*-body solver for determining the dark matter distribution, but these can be handled as force terms in the code. We have developed a scheme to include the dark matter contribution to the gravity by evolving the NFW profile self-consistently with the hydrodynamic evolution of the fluid calculated in the code (Section 2.5). This implementation has an advantage over using the *N*-body solver, in that the dynamics of gas in the NFW dark matter potential can be investigated under controlled conditions. We have also implemented self-gravity of the gas in the code. Dark energy can also be included in the code easily as a force term (Section 2.6). The code is built on modern Godunov-type shock-capturing schemes which are particular suitable for computation of highly supersonic astrophysical flows in the

[2] http://lambda.gsfc.nasa.gov/product/map/dr3/parameters_summary.cfm

presence of strong discontinuities. Shock capturing is needed in our calculations since we are interested in calculating the non-equipartition signatures around the shock regions.

2.2. Boundary Conditions and Computational Domain

The boundary conditions depend on the geometry and the physics of the problem being solved. For a spherically symmetric geometry of the ICM, the inner boundary condition is reflective. Because we are studying the smooth accretion of background materials in isolation, it is natural to use the Hubble-flow-like outer boundary conditions which are defined as

$$\left.\frac{dv_g}{dr}\right|_{\rm in} = \left.\frac{dv_g}{dr}\right|_{\rm out}, \quad (1)$$

$$\rho_{g,\rm in} = \rho_{g,\rm out}, \quad (2)$$

and

$$P_{g,\rm in} = P_{g,\rm out}, \quad (3)$$

where r is the radius, v_g, ρ_g, and P_g are the gas velocity, mass density, and pressure, respectively, and the subscripts "in" and "out" denote the inner and outer quantities at the outer boundary, respectively. Each simulation is set up such that there is an over density in the central region compared to the critical density (Section 2.3). Near the over dense region, materials are accreted toward the center. To avoid boundary effects, the size of the computation domain should be large enough that materials should always be outgoing and follow the Hubble-flow-like outer boundary condition. If the size of the boundary is too small, the dynamics of materials near the boundary would be influenced by the central cluster and would not follow the Hubble-flow-like outflow; in the extreme case, materials should be infalling rather than outgoing. Bertschinger (1985) has shown that in an Einstein–de Sitter universe, materials follow the Hubble-flow-like outflow closely outside of a few times of the turnaround radius (Figure 1(a) therein). The turnaround radius is about 10 Mpc for a cluster with $\sim 10^{15}\,M_\odot$ at present, and hence the estimated radius at where materials follow the Hubble-flow-like outflow is about 30 Mpc from the cluster center. This condition should be sufficient for the ΛCDM universe, since the materials in the ΛCDM universe should be less bounded. To be conservative, in our calculations, we take the boundary radius to be at least a few times this estimated radius. In particular, we take the boundary radius to be 100 Mpc in all models. The outer regions in our calculations at the final time reproduce the observed Hubble flow velocity and the baryon density at redshift zero (Figures 1 and 5 in Sections 4 and 5, respectively), which validates our choice of the outer boundary conditions.

The volume of each simulation was divided into 1000 spherical annuli. The innermost zone width is set to be 0.42 kpc. The widths of the zones increase with radius by a fixed ratio x,

$$dr_{i+1} = x dr_i, \quad (4)$$

where dr_i is the width of the ith zone. The grid is defined such that

$$\sum_{i=1}^{N} dr_i = L, \quad (5)$$

where $N = 1000$ is the total number of zones, and $L = 100$ Mpc is the size of the computational domain. This is called a *stretched grid* in PLUTO. With this grid of radii, the zones near the accretion shock have widths of less than 1% of the shock radius in each simulation from $z = 0$–2. Doubling the resolution gives essentially the same results.

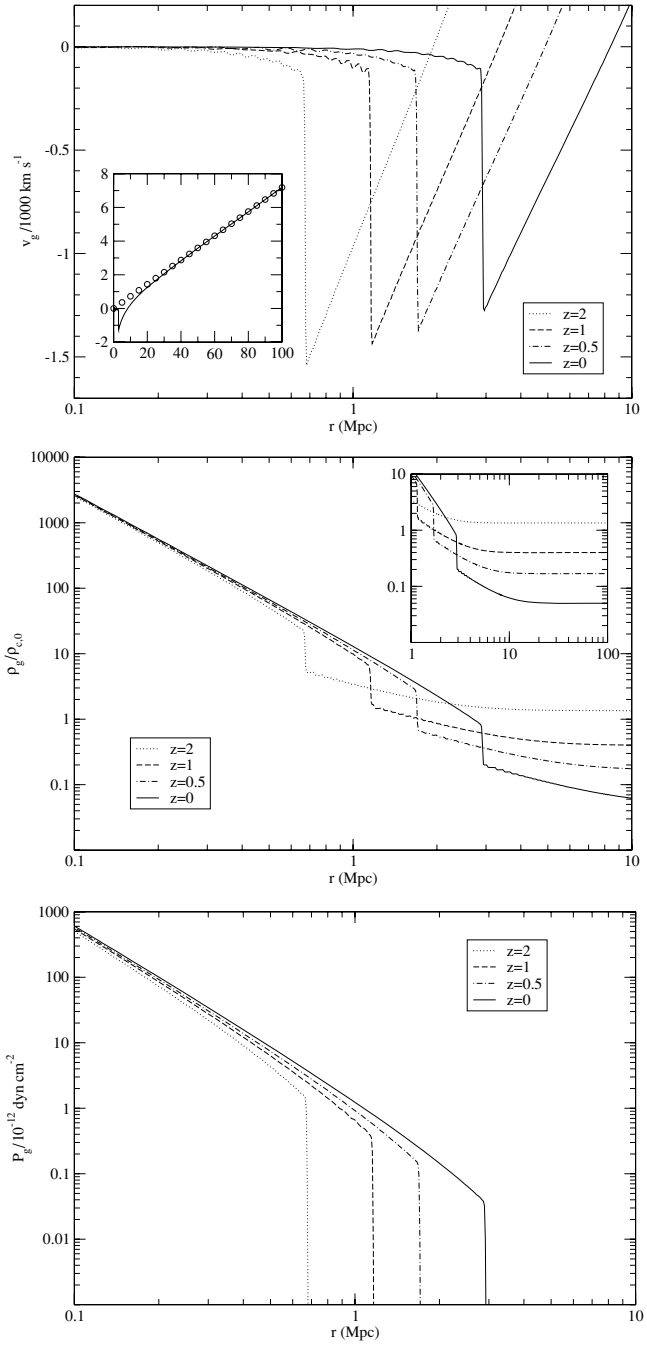

Figure 1. Gas velocity (upper panel), density (middle panel), and pressure (lower panel) profiles of our simulated cluster for the self-similar collisionless dark matter dominated accretion model in the Einstein–de Sitter universe at four different redshifts. The model has a dark matter mass accreted within R_{178} of $M_{178} = 10^{15}\,M_\odot$ at $z = 0$. The insets in the upper and middle panels show the large radius behavior of the gas, with the velocity profile shown for $z = 0$ only. The circles on the inset of the velocity profile give the Hubble flow velocity at $z = 0$. We set $\Omega_b = 0.05$ in this model.

2.3. Initial Conditions for the Realistic NFW Dark Energy Cluster Models

Since at high enough redshift the dynamics of the background universe is close to the Einstein–de Sitter model, the dynamics of a cluster should be close to a self-similar solution as well (Bertschinger 1985). We chose a high initial redshift and set up the initial conditions to be close to the self-similar solution. In particular, the initial condition is such that there are two regions

separated by an accretion shock. The location of the cluster accretion shock in the baryonic material is very close to the first caustic in the dark matter, and the distribution and evolution of the baryonic gas and dark matter are almost identical outside the accretion shock (Bertschinger 1985; Ryu & Kang 1997). Within the shock radius, we assume the dark matter follows the NFW profile (Navarro et al. 1995),

$$\rho_{\rm dm}(r) = \frac{\rho_{\rm dm,s}}{(r/r_s)(1+r/r_s)^2}\,, \tag{6}$$

where $\rho_{\rm dm,s}$ is a density scale and r_s is the scale radius. The scale radius, r_s, is related to the concentration parameter, c, and the virial radius, $r_{\rm vir}$, by

$$r_s = r_{\rm vir}/c\,. \tag{7}$$

The virial radius, $r_{\rm vir}$, is defined by

$$M_{\rm vir} = \frac{4\pi}{3}\Delta_{\rm vir}\rho_c(z) r_{\rm vir}^3\,, \tag{8}$$

where $M_{\rm vir}$ is the virial mass, $\rho_c(z)$ is the critical density of the universe at redshift z, and the critical overdensity $\Delta_{\rm vir}$ is obtained from the solution to the top-hat spherical collapse model, and can be approximated by Bryan & Norman (1998)

$$\Delta_{\rm vir} = 18\pi^2 + 82x - 39x^2 \ \ (\text{for } \Omega_R = 0)\,, \tag{9}$$

where $x \equiv [\Omega_{M,0}(1+z)^3/E(z)^2] - 1$, $E(z)^2 \equiv \Omega_{M,0}(1+z)^3 + \Omega_R(1+z)^2 + \Omega_\Lambda$, and $\Omega_R \equiv 1/(H_0 R)^2$ with R here equals the current radius of curvature of the universe. We adopt a concentration parameter given by Equation (17) in Section 2.4, in which c is effectively equal to 4 in all the initial models considered. We also assume that the gas in the initial models is approximately in hydrostatic equilibrium with the dark matter potential. The choice of such initial conditions is convenient because there exists an analytic solution for isothermal hot gas in hydrostatic equilibrium with the dark matter potential (Makino et al. 1998), but not the total potential. This is convenient for setting up our initial models. In the simulation runs, the self-gravity of gas is indeed included so that such initial models actually deviate from hydrostatic equilibrium slightly. We have checked that the numerical solutions we are interested in are rather insensitive to the set up of the initial conditions, as long as the initial models are approximately in hydrostatic equilibrium. Beyond the shock radius, both the dark matter and the gas follow the self-similar infalling solutions. The initial time (age of the universe) is chosen to be 29.4 Myr, which corresponds to a redshift of $z = 70.6$ in the standard ΛCDM cosmology. The details of the setup are described below.

We first define an initial cluster mass, $M_{{\rm sh},i}$, at the initial time chosen. The initial cluster mass is distributed within an initial shock radius, $R_{{\rm sh},i}$. In the self-similar solution (Bertschinger 1985), $R_{{\rm sh},i}$ and $M_{{\rm sh},i}$ are related by

$$R_{{\rm sh},i} = \lambda_{\rm scale} r_{{\rm ta},i}\,, \tag{10}$$

and

$$M_{{\rm sh},i} = \frac{4\pi}{3}\rho_{c,i}\, r_{{\rm ta},i}^3 m_{\rm scale}\,, \tag{11}$$

where $r_{{\rm ta},i}$ is the initial turnaround radius, $\rho_{c,i}$ is the critical density at the initial time, and, $\lambda_{\rm scale} = 0.347$ and $m_{\rm scale} = 3.54$ are the dimensionless scaled radius and mass in the self-similar solution at the shock radius, respectively. This implies that the initial average overdensity within the accretion shock is

$$\Delta_{{\rm sh},i} = m_{\rm scale}/\lambda_{\rm scale}^3 = 84.73\,. \tag{12}$$

Within the shock radius, we assume the dark matter distribution is given by the NFW profile (Equation (6)). For a fixed value of concentration parameter, $c = 4$ assumed at high redshift (Section 2.4), the initial scale radius $r_{s,i}$ can be solved by using Equation (C9) in Hu & Kravtsov (2003), which is

$$\frac{r_{s,i}}{R_{{\rm sh},i}} = x\left[f_{{\rm sh},i} = \frac{\Delta_{{\rm sh},i}}{\Delta_{{\rm vir},i}} f(1/c)\right], \tag{13}$$

where $f(x) = x^3[\ln(1+x^{-1}) - (1+x)^{-1}]$, $x(f)$ in an accurate fitting form is given in Appendix C in Hu & Kravtsov (2003), and $\Delta_{\rm vir}$ is given in Equation (9). In general, c depends on mass, and r_s can be calculated iteratively. The scale density $\rho_{\rm dm,s}$ in Equation (6) is then fixed by requiring that the total dark matter integrated to the shock radius is equal to $(1 - f_{\rm gas})M_{{\rm sh},i}$.

Within the shock radius, we assume the gas is initially in approximately hydrostatic equilibrium ($v_g = 0$) with the dark matter potential. Initially, the gas is assumed to be isothermal. The gas distribution can be solved analytically, and is given by Makino et al. (1998)

$$\rho_g(r) = \rho_{g,0}\, e^{-27b/2}\left(1 + \frac{r}{r_s}\right)^{27b/(2r/r_s)}\,. \tag{14}$$

The central gas density $\rho_{g,0}$ and b are fixed by simultaneously requiring that the gas fraction within the shock radius is equal to $f_{\rm gas}$ and the gas density at the shock radius is given by the strong shock jump condition

$$\rho_{g2} = 4\rho_{g1}\,, \tag{15}$$

where the subscripts 1 and 2 denote the preshock and postshock quantities, respectively. Once b is fixed, the temperature, and hence the gas pressure is indeed fixed by using Equation (9) in Makino et al. (1998). The gas pressure, P_g, is proportional to ρ_g since the gas is assumed to be isothermal. However, if such pressure profile is used, the pressure at the shock radius does not match the strong shock jump condition in general. This is because the dynamical solution with accretion shock does not follow the isothermal hydrostatic solution given in Makino et al. (1998). Since we are interested in the shock solution in our calculation, we renormalize the gas pressure such that the strong shock jump condition is satisfied at the shock radius,

$$P_{g2} = \frac{4}{3}\rho_{g1}\, v_{g1}^2\,. \tag{16}$$

With this renormalization, the pressure is only lower than the isothermal hydrostatic equilibrium pressure by 17%. The initial gas deviates slight from hydrostatic equilibrium. As long as the gas is in approximately equilibrium initially, the late time evolution of the cluster profiles in the outer regions we are interested in should not be affected by the slightly deviation in the initial condition.

Gas in exact hydrostatic equilibrium with the total gravitational potential satisfying both the density and pressure shock jump conditions is not isothermal in general. We have checked that using initial conditions in exact hydrostatic equilibrium give essentially the same results.

Outside the shock radius, the gas density and velocity profiles are assumed to follow the self-similar infall solution (Bertschinger 1985), and the pressure is set to be effectively zero (i.e., the smallest value the code allows).

2.4. Concentration Parameters

We also need to set the value of the concentration parameter c. Bullock et al. (2001) proposed that c scales as $(1+z)^{-1}$. At low redshift, this is supported by numerical simulations by Wechsler et al. (2002) and Zhao et al. (2003b, 2009), when the dark matter halos are in the slow accretion phase. However, at high enough redshift when the dark matter halos are in the fast accretion phase, the concentration parameter approaches a constant minimum value independent of the mass and redshift of the halo (Zhao et al. 2003a, 2009; Gao et al. 2008). At low redshifts, the variation of the concentration parameter with mass can simply be fitted using a power law (Dolag et al. 2004; Neto et al. 2007). Thus, we adapt the concentration parameter used by Buote et al. (2007) but set a minimum value of 4 (Zhao et al. 2009) independent of the redshift and the halo mass of the cluster in our simulations:

$$c(M_{\rm vir}, z) = \max\left[\frac{c_{14}}{1+z}\left(\frac{M_{\rm vir}}{M_{14}}\right)^{\alpha}, 4\right], \quad (17)$$

where we take $c_{14} = 9.0$ and $\alpha = -0.172$ as determined from the X-ray galaxy clusters with halo masses between $(0.06\text{–}20) \times 10^{14}\, M_{\odot}$ at low redshifts (Buote et al. 2007) and $M_{14} \equiv 10^{14} h_{100}^{-1} M_{\odot}$.

2.5. Self-consistent Evolution of NFW Potential Including Accreted Mass

At each time step, we determine the gas shock radius, and we assume dark matter is distributed according to the NFW profile within the shock radius; outside that radius, the dynamics of dark matter and gas are the same. We assume the baryon fraction is conserved as materials accretes within the shock, and hence, the dark matter mass within the shock radius is equal to $(1/f_{\rm gas} - 1)$ times the gas mass within that region. Although three-dimensional simulations suggest that there is a hydrodynamic outflow of gas and $f_{\rm gas}$ inside a cluster is smaller than the cosmological value, our treatment here is at least self-consistent. Moreover, a smaller value of $f_{\rm gas}$ inside a cluster in reality would enhance the effect of non-equipartition, and hence our calculations give a conservative estimate of the non-equipartition effect. As mentioned in Section 2.3, if the shock radius and the mass within it are known, the dark matter profile can be solved iteratively together with the concentration parameter. The dark matter profile within the shock radius calculated in each time step is used to calculate the gravity contributed by the dark matter within the shock radius.

2.6. Dark Energy Implementation

We will do the calculations in a cosmological background including the accelerated expansion due to dark energy. The accretion of materials depends sensitively on dark energy since it governs the expansion of the background materials which are to be accreted (Ryu & Kang 1997). To implement dark energy in the one-dimensional Newtonian code, we utilize the similarity between the Friedmann solution and Newtonian cosmology, since the latter can be solved in the Newtonian code. The dynamical solution of the scale factor, a, of a homogeneous universe is governed by

$$\ddot{a} = -\frac{4\pi G}{3} a \left(\rho + \frac{3P}{c^2}\right), \quad (18)$$

where ρ and P are the total energy density and pressure of the universe, respectively, and G and c are the gravitational constant and speed of light, respectively. The Newtonian analog is simply replacing a by r, i.e.,

$$\frac{d^2 r}{dt^2} = -\frac{4\pi G}{3} r \left(\rho + \frac{3P}{c^2}\right). \quad (19)$$

For a pure dark energy universe where the dark energy is described by the cosmological constant Λ, $\rho = \rho_{\Lambda}$, $P = P_{\Lambda}$, and $\rho_{\Lambda} = -P_{\Lambda}/c^2$. Thus, Equation (19) becomes

$$\frac{d^2 r}{dt^2} = \frac{8\pi G}{3} \rho_{\Lambda} r. \quad (20)$$

We identify the right-hand side of Equation (20) to be the repulsive force per unit mass contributed by the dark energy. The dark energy density, ρ_{Λ}, in the ΛCDM cosmology is constant throughout the history of the universe, and is given by

$$\rho_{\Lambda} = \Omega_{\Lambda,0}\, \rho_{c,0}, \quad (21)$$

where the quantities on the right-hand side are evaluated at the present time. With the force term in Equation (20) implemented into the code, the baryon density of the background cosmology is reproduced correctly in each of our simulations (see Figure 5 below).

3. ELECTRON HEATING WITHIN A CLUSTER

3.1. General Picture of Shock Heating and the Equilibration between Electrons and Ions Afterward

The heating of electrons passing through a shock within a cluster involves at least a two-step process. The first step is the shock heating of electrons within the very narrow shock, and the second step is the equilibration between electrons and ions afterward. In this section, we outline the general picture of electron heating within a cluster we assumed for our model. The detailed implementations of the shock heating (first step) and the Coulomb equilibration afterward (second step) are presented in Sections 3.2 and 3.3, respectively. Section 3.4 outlines the steps to calculate electron heating in our code.

Immediately after the infalling material (electrons and ions, together with dark matter) has passed through a collisionless accretion shock, we assume it should primarily heat the ions rather than electrons since they carry most of the kinetic energy of the infalling gas. The electron temperature immediately behind the shock would be lower than the ion temperature, and they would be in a state of non-equipartition. Indeed, non-equipartition of ions and electrons is known in various astrophysical shocks. Most supernova remnants with high Mach numbers comparable to cluster accretion shocks have electron temperatures which are lower than the ion temperatures (Ghavamian et al. 2007); in situ measurements from satellites show the same feature in the Earth's bow shock (Hull et al. 2001). It is reasonable to assume that cluster accretion shocks are similar to those astrophysical shocks. Within the very narrow shock region, electrons and ions can exchange energy by collisionless processes generated by plasma instabilities there. Unfortunately, the collisionless heating mechanisms and the rate of heating are still poorly known theoretically. We simply model the shock heating efficiency for the electron as a free parameter (Section 3.2).

After the electrons and ions have passed through the thin shock front, they will then be equilibrated by Coulomb collisions (Bykov et al. 2008a, 2008b). It is also possible that behind

the shock, electrons and ions can exchange energy by collisionless processes generated by plasma instabilities left behind. Again, the collisionless heating mechanisms and the rate of equilibration are still poorly known theoretically. It has been argued that behind a strong shock, the spectra of supernova remnants are consistent with purely Coulomb equilibration processes (Rakowski et al. 2003). Given both the theoretical uncertainty concerning the collisionless heating mechanisms and at least some observational evidence that collisionless processes are not important in the equilibration downstream, we simply consider the Coulomb collisions as the only equilibration process behind the shock in our calculations (Section 3.3).

In calculating the equilibration processes of electrons and ions, we consider a fully ionized plasma of hydrogen and helium only. The timescale for charged particles of the same species to achieve a Maxwellian distribution can be estimated by the collisional timescale (Spitzer 1962, p. 133)

$$t_{xx} = 28.6\,\mathrm{Myr}\left(\frac{T_x}{10^7\,\mathrm{K}}\right)^{3/2}\left(\frac{n_x}{10^{-5}\,\mathrm{cm}^{-3}}\right)^{-1}\left(\frac{\ln\Lambda}{40}\right)^{-1}\frac{A_x^{1/2}}{Z_x^4}, \quad (22)$$

where T_x is the temperature of the species x after it has achieved equilibrium, n_x is the number density, A_x is the particle mass number, Z_x is the particle charge, and $\ln\Lambda$ is the Coulomb logarithm which is similar for all species of interest. For the charged particles we are interested in, the electron–electron collisional timescale is the shortest, with $t_{ee} \sim t_{pp}A_e^{1/2} \sim t_{pp}/43$. For typical abundance $n_{\rm H} \sim 10n_{\rm He}$, $t_{pp} \sim t_{\rm He^{+2}He^{+2}}$. For protons, the collisional timescale is $t_{pp} \sim 30$ Myr, which is much shorter than the age of the cluster or the accretion timescale. For an accretion shock propagating outward with a velocity $v_s \sim 1000$ km s^{-1}, protons at a distance $d \sim v_s t_{pp}/4 \sim 7$ kpc away from the shock should be in a Maxwellian distribution. This is of the order of the zone size ($\sim$10 kpc) at the shock radius in our calculations. Hence, we can assume that protons, helium ions, and electrons are in equilibrium independently with temperatures T_p, $T_{\rm He^{+2}}$, and T_e, respectively. The energy exchange timescale for two species of particles, x and y in Maxwellian distributions with temperatures T_x and T_y is given by the equilibration timescale (Spitzer 1962, p. 135)

$$t_{xy} = 14.7\,\mathrm{Myr}\left(\frac{T_x}{10^7\,\mathrm{K}}\right)^{3/2}\left(\frac{n_y}{10^{-5}\,\mathrm{cm}^{-3}}\right)^{-1}\left(\frac{\ln\Lambda}{40}\right)^{-1} \times \frac{A_y}{Z_x^2 Z_y^2 A_x^{1/2}}\left(1+\frac{T_y}{T_x}\frac{A_x}{A_y}\right)^{3/2}. \quad (23)$$

Consider energy exchange between electrons and protons, and assume that the electrons are initially much cooler than the protons. When $T_e \lesssim T_p(m_e/m_p)$, the electrons are heated rapidly, with $t_{ep} \sim t_{pp}/3600$. Thus, we expect that most of the time spent in electron heating will occur in the regime in which $T_e/T_p \gg m_e/m_p$. Hence, the energy exchange timescale between electrons and protons, t_{ep} is on the order of $0.5(m_p/m_e)^{1/2}t_{pp} \sim 21t_{pp}$. Similarly, $t_{e\rm He^{+2}} \gtrsim t_{ep}$ for $n_{\rm H} \sim 10n_{\rm He}$. The equipartition timescale between electrons and ions (either protons or helium ions) will be of the order of 0.6 Gyr, which is comparable to the accretion timescale of a cluster, ((cluster size)/(accretion velocity)) $\sim$1 Gyr. Thus, T_e may not be equal to T_p or $T_{\rm He^{+2}}$ in the outer regions of a cluster, which is the problem we are considering. From Equation (23), it can be seen that $t_{\rm He^{+2}p} \gtrsim t_{pp}$. It is also possible that $T_p \neq T_{\rm He^{+2}}$ in the regions of interest. The solutions of the equilibration of the plasma formally can be obtained by solving the equilibration between the three species. If we are interested only in the electron temperature evolution, we can consider the energy exchange rate between the electrons and both of the two ion species

$$1/t_{ei} = 1/t_{ep} + 1/t_{e\rm He^{+2}}. \quad (24)$$

Since the contribution per ion to t_{ei}^{-1} is the same for protons and helium ions (Equation (23)), the rate of change of electron temperature with the plasma, dT_e/dt, depends only on the mean ion temperature (Fox & Loeb 1997). Moreover, once the ions reach equilibrium with each other, the rate of change of their temperatures due to collisions with electrons is the same, so they will remain in equilibrium. Thus, for simplicity, we assume a single ion temperature, T_i, and we assume the electrons with temperature T_e are equilibrated with this single ion temperature plasma.

In hydrodynamic simulations, the three hydrodynamic variables, the gas mass density, ρ_g, the total gas pressure, P_g, and the gas velocity, v_g, determine the hydrodynamic state of the fluid completely, independent of the kinetic state of the plasma. Since we are interested in the difference between electron temperature, T_e, and ion temperature, T_i, we assign a new variable, $\tau \equiv T_e/\bar{T}$, in each grid of our hydrodynamic calculations, where $\bar{T}$ is the average thermodynamic temperature of the fluid given by $\bar{T} \equiv (\mu m_p/k_B)(P_g/\rho_g)$, where $\mu = 0.59$ is the mean molecular weight, m_p is the proton mass, and k_B is the Boltzmann constant. The electron temperature, T_e, the ion temperature, T_i, and the average thermodynamic temperature, $\bar{T}$, are simply related by

$$\bar{T} = \frac{n_e T_e + n_i T_i}{n_e + n_i}, \quad (25)$$

where n_e and n_i are the electron and ion number densities, respectively.

3.2. Electron Heating within the Thin Shock Front

Within the very narrow shock front, electrons can be heated by both adiabatic compression and non-adiabatic heating. Non-adiabatic heating includes the conversion of the bulk kinetic energy into thermal energy and other collisionless heating processes generated by plasma instabilities. We can define the total non-adiabatic electron heating efficiency in the shock, β, to be the change in electron temperature due to non-adiabatic heating, $\Delta T_{e,\rm non-ad}$, relative to the change in average thermodynamic temperature due to non-adiabatic heating, $\Delta\bar{T}_{\rm non-ad}$,

$$\beta \equiv \left(\frac{\Delta T_e}{\Delta\bar{T}}\right)_{\rm non-ad}. \quad (26)$$

The change in the bulk kinetic energy per particle is $m(v_{g1}^2 - v_{g2}^2)/2$, where m is the particle mass, and hence the increase in the electron temperature is much smaller than that of the ions in a shock. For the electron heating processes generated by plasma instabilities, the details of the mechanism and the efficiency are still unclear. Therefore, in our study, we assume total non-adiabatic electron heating efficiency, β, to be a constant for any given cluster model. Adiabatic compression increases the electron temperature by a factor of $(\rho_{e2}/\rho_{e1})^{\gamma-1}$, where γ is the adiabatic index, ρ_{e1} and ρ_{e2} are the preshock and postshock electron temperatures, respectively. For a strong shock with $\gamma = 5/3$, adiabatic compression only increases the electron temperature by a factor of $2^{4/3} \approx 2.5$. Thus, if the preshock electron temperature, T_{e1}, is negligible compared to the postshock average

temperature, $\bar{T}_2$, adiabatic heating would not be important. This is indeed the case in our models. Nevertheless, we have included adiabatic heating in our calculations. Including both adiabatic and non-adiabatic heating, the postshock electron temperature immediately after the shock is given by (the Appendix)

$$T_{e2} = \left(\frac{\rho_{g2}}{\rho_{g1}}\right)^{\gamma-1} T_{e1} + \beta \max\left[0, \bar{T}_2 - \left(\frac{\rho_{g2}}{\rho_{g1}}\right)^{\gamma-1} \bar{T}_1\right], \quad (27)$$

where a minimum of zero in the second term is set to ensure that numerical fluctuations do not introduce a false decrease in entropy in the non-adiabatic heating.

Note that we assume that the heating of electrons is equivalent to the increase of temperature. This is only true if the electron distribution is Maxwellian. The time for the electrons to achieve a Maxwellian distribution after they have been heated at the shock is $t_{ee} \sim t_{pp}/43 \sim 0.7\,\mathrm{Myr}$ (Section 3.1). As shown in Section 3.1, this is much shorter than the accretion timescale, and the electrons within the zone size at the shock radius of our simulations should achieve the Maxwellian distribution. Note also that even if electrons are in non-Maxwellian distribution and if such electrons are heated much faster than the Coulomb collisional heating rate, the faster heating within the shock has already been parameterized by the electron heating efficiency β.

Recently, observations of supernova remnants have shown that the electron heating efficiency at the shock is inversely proportional to the Mach number squared (Ghavamian et al. 2007). If the result can be applied to cluster accretion shocks, the high accretion shock Mach number ($\mathcal{M} > 100$) would imply the electron heating efficiency to be $\ll 1$ in cluster accretion shocks. In our work, we consider two cases for the shock heating of electrons: $\beta = 1/1800$ (the mass ratio of electrons to protons) as a model for a very low non-adiabatic heating efficiency which is supported by supernova remnant observations, and $\beta = 0.5$ as a model for an intermediate heating efficiency within the shock.

3.3. Coulomb Equilibration After Shock Heating

After the shock-heated material has passed through the thin shock front, we assume Coulomb equilibration as the only heating process for electrons behind the shock. The evolution of electron temperature due to Coulomb collision is given by (Spitzer 1962, p. 135)

$$\frac{d\tau}{dt} = \frac{2\ln\Lambda}{503}\left\langle\frac{Z^2}{A}\right\rangle \frac{n}{\bar{T}^{3/2}}\tau^{-3/2}(1-\tau)\,\mathrm{s}^{-1}, \quad (28)$$

where n is the total particle number density, $\ln\Lambda \approx 37.8 + \ln(T_e/10^8\,\mathrm{K}) - \ln(n_e/10^{-3}\,\mathrm{cm}^{-3})^{1/2}$ is the Coulomb logarithm, the angle bracket term is the mean value over the ratio of the square of ion charge Z and the atomic number A. For our model of a pure hydrogen and helium gas, the angle bracket term equals 1 as long as $T_e/T_i \gtrsim m_e/m_p$, which is true for our models with a minimum $\beta = 1/1800$. We solve Equation (28) for each time step in our hydrodynamic calculations (Section 3.4).

3.4. Steps to Calculate the $T_e/\bar{T}$ Evolution

Cosmological accretion shocks are identified as shocks in which the Mach number, $\mathcal{M}$, is greater than 10. In our simulations, we use the pressure shock jump condition,

$$\frac{P_{g2}}{P_{g1}} = \frac{2\gamma}{\gamma+1}\mathcal{M}^2 - \frac{\gamma-1}{\gamma+1}, \quad (29)$$

to identify shocks. In each time step of our hydrodynamic simulations, if the condition of $\mathcal{M} > 10$ in Equation (29) is satisfied, we identify there is a strong shock at r_2. We found that this condition can identify cosmological shocks correctly in our simulations. In regions without a strong shock, we calculate the $T_e/\bar{T}$ evolution using Equation (28) throughout the entire time step. If an accretion shock is identified, we first use Equation (28) to evolve $T_e/\bar{T}$ for one half of the time step. Then, we apply the shock heating using Equation (27). Finally, we use Equation (28) again to evolve $T_e/\bar{T}$ for the reminding half of the time step.

Cosmological simulations show that there are various kinds of shocks formed in the LSSs (Kang et al. 2007). Based on their location, these shocks can be classified as external and internal shocks. External shocks are formed around the outermost surfaces of the LSSs that unshocked intergalactic gas is falling onto (sheets, filaments, and halos), and the gas is shock heated for the first time. These external shocks in general have Mach numbers $\gg$10. Internal shocks have low Mach numbers $\lesssim$10. They are formed within those nonlinear structures, e.g., galaxy clusters and filaments, by the infall of previously shocked gas during subclump mergers, as well as by chaotic flow motions. These cosmological simulations show that there are a large number of low Mach number internal shocks contributing significantly to the thermal energy budget of a cluster (Kang et al. 2007). Since those small Mach number internal shocks are mainly found well within inner regions of a cluster where the densities are high enough, electrons and ions are in general in equipartition. Here, we are only interested in the non-equipartition effects of electrons and ions, and these effects are only significant in very low density regions (e.g., cosmological accretion shock regions) rather than the contribution of the thermal energy from the shocks to the cluster. For our one-dimensional simulations which are used to study relaxed clusters, due to the symmetry of the problem, there is in fact only one cosmological accretion shock with Mach number $\gg$10 for each cluster, and there are no internal shocks formed. For comparison, three-dimensional simulations have shown that for relaxed clusters, the number of small Mach number internal shocks is much smaller than that of the high Mach number external shocks (Molnar et al. 2009). This is because internal shocks are formed mostly by mergers or chaotic flow motions which are less likely to be found in relaxed clusters by definition. Thus, we do not have to consider electron heating by the low Mach number internal shocks at least for relaxed cluster that we are interested in. Future three-dimensional simulations will be needed to test our assumption.

4. TEST MODELS: SELF-SIMILAR MODELS

The essential physics governing the equilibration problem we are considering are the hydrodynamics of the gas, the gravity by both dark matter and gas, the equilibration physics between electrons and ions, as well as the dark energy which modifies the background cosmology, and hence the rate of accretion onto clusters and the duration of the accretion throughout cosmic history. The contribution of dark energy can be tested by whether the baryon density of the background cosmology can be reproduced correctly in each of our simulations, and this is indeed the case for our realistic simulations which will be presented in Section 5 (see Figure 5 below). We present three tests here to show that our hydro code can handle the necessary physics correctly for the problem we are considering. The hydrodynamical response of the gas in an

external gravitational field is tested by reproducing the analytic self-similar solutions of a collisionless dark matter dominated accretion model (Bertschinger 1985). The correct handling of self-gravity of the gas is tested by reproducing the analytic self-similar solutions of a collisional gas dominated accretion model (Bertschinger 1985). Finally, the correct handling of the equilibration physics is tested by comparing to the analytic solutions of a self-similar non-equipartition model calculated by Fox & Loeb (1997).

4.1. Collisionless Dark Matter Dominated Accretion Model

In this section, we compare our numerical simulation with the analytic self-similar solution of the collisionless dark matter dominated accretion model in the Einstein–de Sitter universe ($\Omega_M = 1, \Omega_\Lambda = 0$). In this model, we assume gravity is dominated by the dark matter potential, and hence the self-gravity of the gas is switched off in the code. This is done to test the ability of our code to handle an external gravitational potential, which is important for our realistic simulations with the NFW dark matter potential included. We set Ω_b to be 0.05 in this model. We assume the current Hubble constant to be $H_0 = 71.9$ km s^{-1} Mpc^{-1} in this simulation run, and hence at redshift $z = 0$, the critical density is $\rho_c(z = 0) = 9.71 \times 10^{-30}$ g cm^{-3}. The initial gas profiles are set according to the self-similar solution given in Bertschinger (1985). The gravitational potential due to the dark matter is calculated according to the self-similar solution at each time step. The gas evolution within the dark matter gravitational potential is then calculated by the PLUTO code. Figure 1 shows the dynamical variables of our numerical simulations for the self-similar model at four different redshifts. The model shown in the three panels is such that the dark matter mass accreted within R_{178} is $M_{178} = 10^{15}\,M_\odot$ at $z = 0$. The figure shows that a strong shock is propagating from $R_{\rm sh} \approx 0.7$ Mpc at $z = 2$ to $R_{\rm sh} \approx 3$ Mpc at $z = 0$. The shock velocity decreases from $v_{\rm sh} \approx 1500$ km s^{-1} at $z = 2$ down to $v_{\rm sh} \approx 1300$ km s^{-1} at $z = 0$. At $z = 0$, the gas density just within the shock is about $0.8\rho_c(z = 0)$, and drops to about $0.2\rho_c(z = 0)$ just beyond the shock, while a very sharp jump in pressure can be seen at the shock radius. At about 100 Mpc, which is at the edge of our simulation domain, the density drops according to the background cosmology as $\Omega_b\rho_c$ (inset in the middle panel of Figure 1). The velocity profile at very large radii also follows the Hubble flow (inset in the top panel of Figure 1).

To compare with the analytic self-similar solution directly, we scale the physical radius and the dynamical variables to obtain the scaled dimensionless valuables according to the scaling relations given in Bertschinger (1985),

$$\begin{aligned} \lambda &= r/r_{\rm ta}\,, \\ \upsilon(\lambda) &= \frac{v_g(r,t)}{r_{\rm ta}/t}\,, \\ \phi(\lambda) &= \frac{\rho_g(r,t)}{\rho_c\Omega_b}\,, \\ \psi(\lambda) &= \frac{P_g(r,t)}{\rho_c\Omega_b r_{\rm ta}^2/t^2}\,, \end{aligned} \tag{30}$$

where λ, υ, ϕ, and ψ are the dimensionless radius, velocity, density, and pressure of the gas, respectively, t is the cosmic time which is equal to $1/\sqrt{6\pi G\rho_c}$ for the Einstein–de Sitter universe. The scaled dimensionless valuables in our simulation are shown as solid lines in Figure 2. The analytic solutions are plotted as open circles for comparison. After scaling, the dimensionless valuables in our simulation at the four different redshifts, as well as the analytic solutions, all lie almost along the same locus which can hardly be distinguished on the figures. This shows that our numerical simulations are in excellent agreement with the analytic solutions within all region of our interest (∼0.1–10 Mpc). We conclude here that our code can calculate the dynamics of the gas, as well as handling the shock in an external gravity under the cosmological expansion correctly.

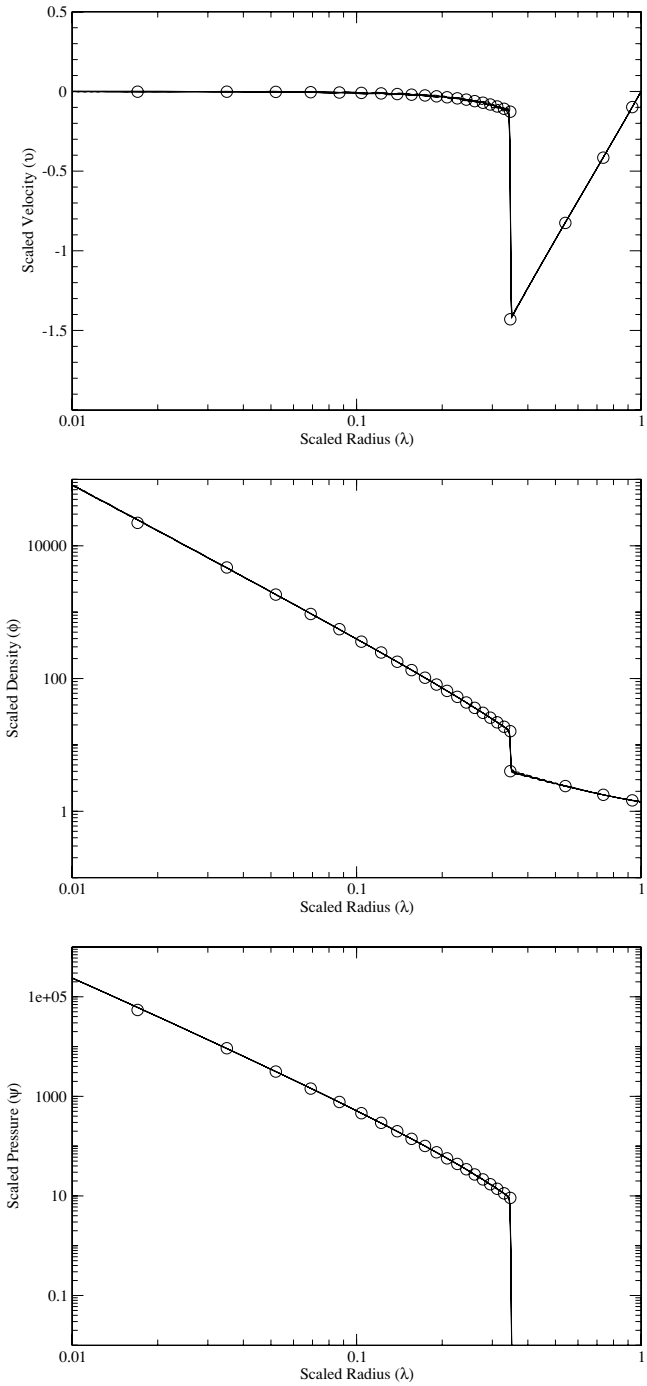

Figure 2. Scaled gas velocity (upper panel), density (middle panel), and pressure (lower panel) profiles of our simulated cluster. The hydrodynamic model is the same as in Figure 1. All four lines lie almost on top of one another in the figures. Circles show the corresponding analytic solutions.

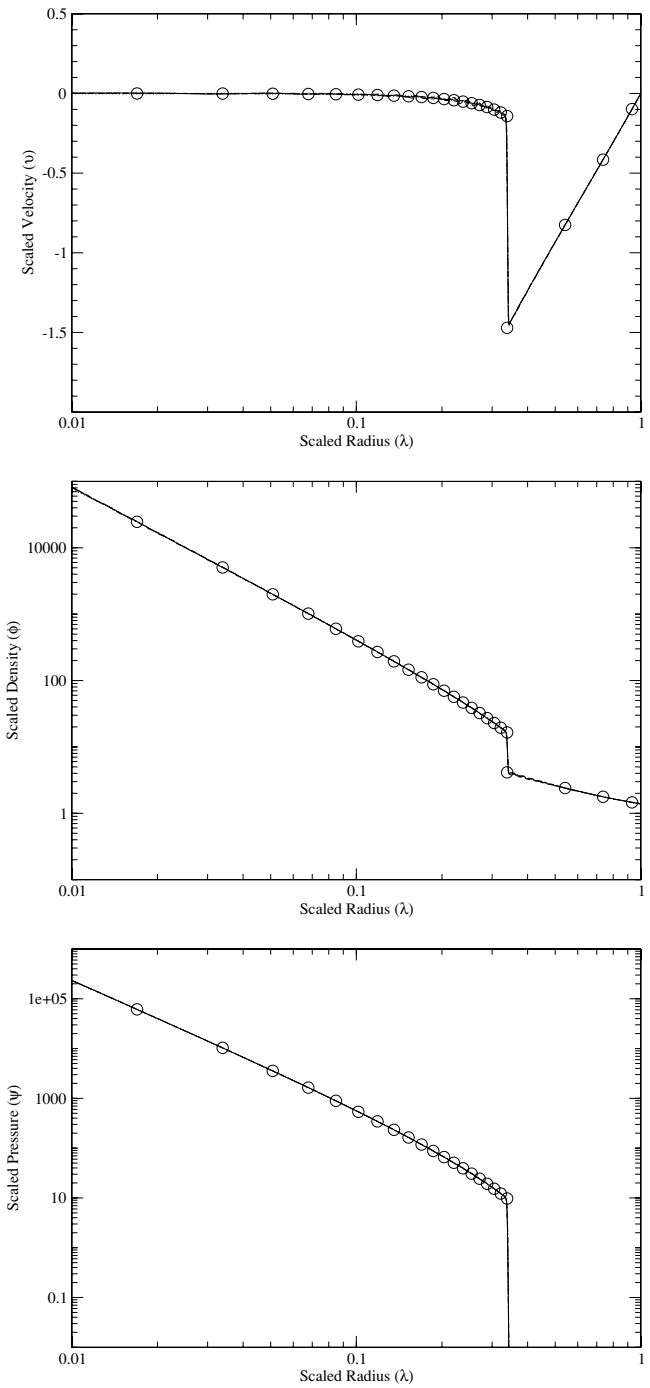

Figure 3. Similar to Figure 2 but for the self-similar collisional gas dominated accretion model in the Einstein–de Sitter universe. The model has a gas mass accreted within R_{178} of $M_{178} = 1.18 \times 10^{15}\,M_{\odot}$ at $z = 0$.

4.2. Collisional Gas Dominated Accretion Model

Since we have included self-gravity of the gas in our realistic simulations, it is necessary to check whether our code can handle self-gravity correctly. We have performed a set of simulations to compare with the analytic self-similar solution of the collisional gas accretion model in the Einstein–de Sitter universe ($\Omega_M = \Omega_b = 1, \Omega_\Lambda = 0$). In this model, the universe is considered as purely collisional fluid, and hence we do not include the dark matter contribution in these simulations. Self-gravity of the gas is included in the simulations. We scaled the physical radius and the dynamical variables according to

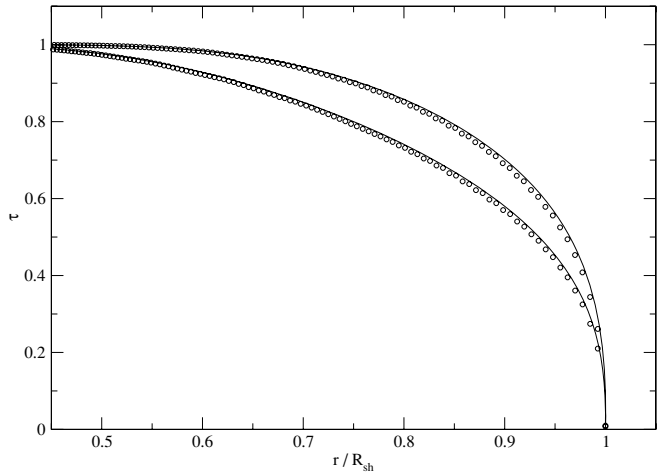

Figure 4. Ratios of the electron and average thermal dynamic temperature, τ, as a function of scaled radius $r/R_{\rm sh}$ for clusters of the self-similar collisionless dark matter dominated accretion model in the Einstein–de Sitter universe at $z = 0$. The upper and lower solid lines are the analytic solutions for cluster masses with $M_{178} = 5.26 \times 10^{14}\,M_{\odot}$ and $M_{178} = 1.05 \times 10^{15}\,M_{\odot}$, respectively. The open circles on the corresponding lines are our simulated results. We assume $\Omega_b = 0.05$ here.

Equation (30) with $\Omega_b = 1$. The scaled dimensionless valuables in our simulations are shown as the solid lines of Figure 3. The analytic solutions are plotted as open circles for comparison. Again, the figure shows that our numerical simulations are in excellent agreement with the analytic solutions. We conclude here that our code can calculate the dynamics of the gas, as well as handle the shock with self-gravity under the cosmological expansion correctly.

4.3. Self-similar Non-equipartition Model

With the self-similar dynamical cluster model calculated in Section 4.1 from our simulations, we can calculate the degree of non-equilibration of the gas following the method given in Section 3. In Figure 4, the ratios of the electron and average thermodynamic temperature, τ, for two clusters with different masses are shown as circles. The corresponding lines are the analytic solutions (Fox & Loeb 1997). Our simulations are in very good agreement with the analytic solutions. The slightly deviations are mainly due to the finite resolution of the shock region in our numerical simulations. We conclude here that our code can calculate the equilibration physics correctly.

5. DYNAMICS FOR REALISTIC NFW DARK ENERGY MODELS

Table 1 lists the masses and radii for different overdensities for some representative NFW cluster models in the standard ΛCDM cosmology at $z = 0$. The different definitions of masses and radii are used interchangeably throughout the paper. In Figure 5, we show the evolution of the dynamical variables (v_g, ρ_g, and P_g) as a function of radius for a cluster with an accreted mass of $M_{\rm vir} = 1.19 \times 10^{15}\,M_{\odot}$ at $z = 0$, where $M_{\rm vir} = M_{95}$ in the ΛCDM cosmology we assumed. The total mass within the shock radius is $M_{\rm sh} = 1.53 \times 10^{15}\,M_{\odot}$ at $z = 0$. The figure shows that a strong shock propagates from $R_{\rm sh} \approx 1.2$ Mpc at $z = 2$ to $R_{\rm sh} \approx 4.2$ Mpc at $z = 0$. The shock velocity decreases from $v_{\rm sh} \approx 1400$ km s^{-1} at $z = 2$ down to $v_{\rm sh} \approx 1000$ km s^{-1} at $z = 0$. Similarly to the self-similar dark matter dominated model, at $z = 0$, the gas density just within the

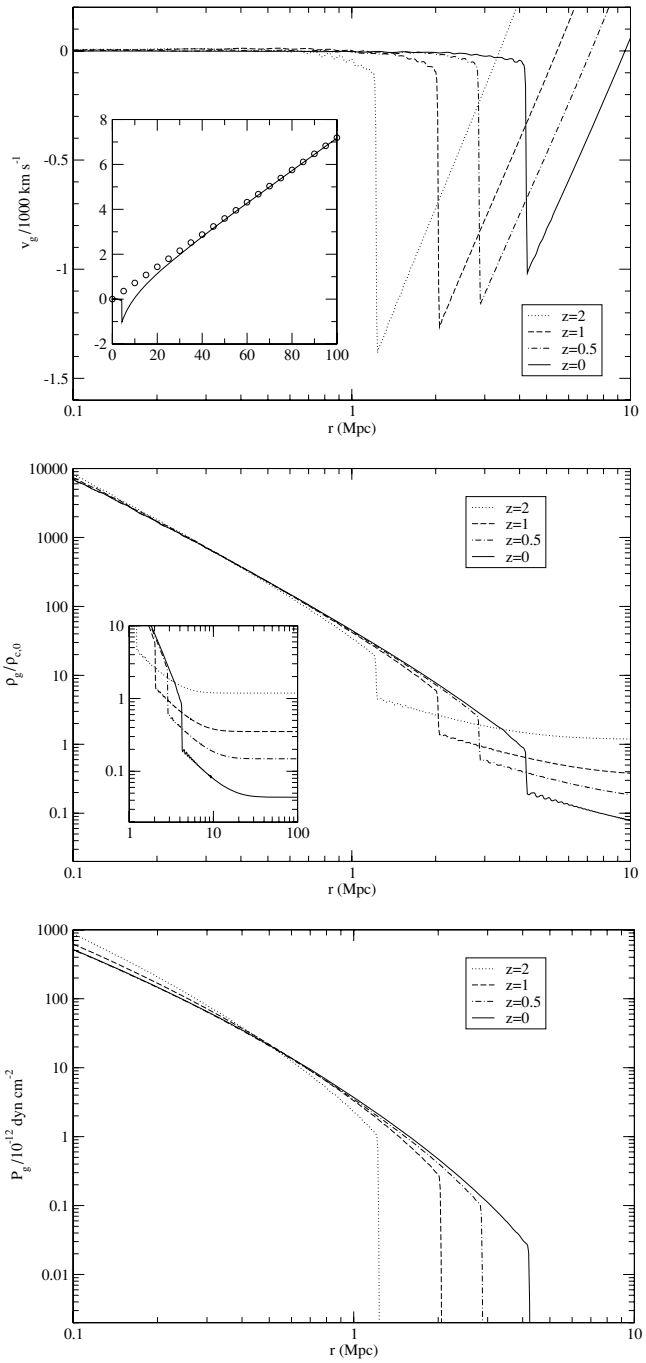

Figure 5. Gas velocity (upper panel), density (middle panel), and pressure (lower panel) profiles of our simulated cluster for the realistic NFW dark energy model in the standard ΛCDM universe at four different redshifts. The model has total mass accreted within $R_{\rm sh}$ of $M_{\rm sh} = 1.53 \times 10^{15}\,M_\odot$ at $z = 0$. The insets show the large radius behavior of the gas, with the velocity profile shown for $z = 0$ only. The circles on the inset of the velocity profile give the Hubble flow velocity at $z = 0$.

shock is about $0.8\rho_c(z = 0)$, and drops to about $0.2\rho_c(z = 0)$ just beyond the shock. At about 100 Mpc which is at the edge of our simulation domain, the density drops according to the background cosmology as $\Omega_b\rho_c$ (inset in the middle panel of Figure 5). The pressure profile flattens as the NFW cluster evolves, and the central pressure drops. This is in contrast to the self-similar dark matter dominated model where the pressure never drops even in the very central region <0.1 Mpc (not shown on the graph). The velocity profile at large radius also

Table 1
Masses and Radii[a] of Some Representative NFW Cluster Models in the Standard ΛCDM Cosmology at $z = 0$

$M_{\rm sh}$	$R_{\rm sh}$	$M^{\rm b}_{\rm vir}$	$R_{\rm vir}$	M_{200}	R_{200}	M_{500}	R_{500}
7.65	3.31	6.05	2.19	4.90	1.60	3.59	1.06
15.3	4.22	11.9	2.75	9.50	1.99	6.83	1.32
30.6	5.41	23.1	3.43	18.3	2.48	12.9	1.63

Notes.
[a] Masses are in the unit of $10^{14}M_\odot$ and radii are in the unit of Mpc.
[b] $\Delta_{\rm vir} = 95.3$ at $z = 0$ for the standard ΛCDM cosmology.

follows the Hubble flow correctly (the inset of Figure 5). This shows that with our implementation of the dark energy, our simulations can reproduce the background cosmology correctly. For comparison, the shock radius and the shock velocity for a self-similar dark matter dominated cluster with the same mass ($M_{\rm sh}$) in the Einstein–de Sitter universe ($\Omega_M = 1, \Omega_\Lambda = 0$) are $R^{\rm SS}_{\rm sh} = 3.11h^{-2/3}_{71.9}(M_{\rm sh}/1.53 \times 10^{15}M_\odot)^{1/3}$ Mpc and $v^{\rm SS}_{\rm sh} = 1.38 \times 10^3 h^{1/3}_{71.9}(M_{\rm sh}/1.53 \times 10^{15}\,M_\odot)^{1/3}$ km s^{-1}, respectively. For the realistic NFW dark energy model, the shock radius is larger than that of the self-similar solution by a factor of 1.38, while the shock velocity is lower by a factor of 1.35. The result is consistent with the one-dimensional *N*-body simulation given by Ryu & Kang (1997). Their results show that the shock radius and the shock velocity for a cluster in the ΛCDM cosmology with $\Omega_\Lambda \approx 0.74$ is about 1.4 larger and 1.35 lower than those in the Einstein–de Sitter universe, respectively.

6. OBSERVABLES FOR REALISTIC NFW DARK ENERGY MODELS

6.1. Definition of X-ray Observables

X-ray spectra depend mainly on electron temperature rather than ion temperature, and the projected temperature profile of a cluster can be directly measured from X-ray observations. Different weighting schemes have been used to calculate the projected temperature from hydrodynamic simulations, and Mazzotta et al. (2004) have shown that most of the commonly used weighting schemes (the mass-weighted and the emission-weighted) give significantly different results from the X-ray observed spectroscopic temperature, $T_{\rm spec}$, and the spectroscopic-like temperature calculated from an analytic weighting scheme they developed is able to approximate $T_{\rm spec}$ to better than a few percent for temperature above ∼3 keV. However, for the non-equipartition model we considered, the electron temperature in the outer regions can be as low as 0.1 keV. X-ray line emission from heavy elements contribute significantly to the X-ray spectrum for temperature below ∼3 keV. Such line emission is not considered by Mazzotta et al. (2004). Vikhlinin (2006) has generalized the spectroscopic-like temperature to lower temperatures down to ∼0.5 keV and to arbitrary metallicity. This generalized scheme takes into account both the continuum and line emission assuming the MEKAL emission model (Mewe et al. 1985; Kaastra & Mewe 1993; Liedahl et al. 1995). The detector response has also been taken into account. The weighting scheme is no longer analytic and has to be tabulated. Following the algorithm of Vikhlinin (2006), we calculate the projected spectroscopic-like temperature, $T_{\rm sl}$, from our numerical simulations. The integration is carried out within the shock radius. The latest *Chandra* ACIS-S aim point response files released for the ACIS Cycle 11 proposal planning are used to generate the

weighting table.[3] Using different *Chandra* CCD response files does not affect the results significantly (Vikhlinin 2006).

We also calculate the surface brightness profile from our numerical simulations. Here, we define x as the projected radial distance from a cluster center. The surface brightness profile in a given energy band E is given by

$$S_E(x) = \int \Lambda_E(T_e, Z) n_e n_p dl \,, \tag{31}$$

where $\Lambda_E(T_e, Z)$ is the cooling function which depends only on the electron temperature and heavy element abundances, Z, n_p is the proton number density, and l is the distance along the line of sight. The integration is carried out within the shock radius. The cooling function $\Lambda_E(T_e, Z)$ is calculated using the MEKAL model (Mewe et al. 1985; Kaastra & Mewe 1993; Liedahl et al. 1995).

For our models with non-equipartition considered, T_e is used to calculate the $T_{\rm sl,non\text{-}eq}$ and $S_{E,\rm non\text{-}eq}$. For comparison, we also consider models with electrons and ions are fully in equipartition by taking $T_e = \bar{T}$, which is usually assumed in the literature. Quantities calculated with full equipartition assumed are denoted with the subscript "eq."

Note that in the outer region where electrons and ions may not be in equipartition, non-equilibrium ionization may also be important. This may increase line emissions in the soft bands ($E \lesssim 1$ keV). In our calculations, non-equilibrium ionization is not considered.

6.2. Definition of SZ Observables

The SZ effect by a cluster at x can be characterized as a temperature increment, $\Delta T_{\rm SZE}(x)$, with respect to the CMB spectrum

$$\Delta T_{\rm SZE}(x) = f(\theta) y(x) T_{\rm CMB} \,, \tag{32}$$

where $\theta = h\nu / k_B T_{\rm CMB}$ is the dimensionless frequency, $T_{\rm CMB}$ is the CMB temperature, y is the Comptonization parameter, and $f(\theta)$ is given by

$$f(\theta) = \left(\theta \frac{e^\theta + 1}{e^\theta - 1} - 4 \right) [1 + \delta_{\rm SZE}(\theta, T_e)] \,. \tag{33}$$

For simplicity, we neglect the relativistic term, $\delta_{\rm SZE}$, which is not important for frequency lower than about 250 GHz. The Comptonization parameter is given by

$$y = \frac{k_B \sigma_{\rm T}}{m_e c^2} \int n_e T_e dl \propto \int P_e dl \,, \tag{34}$$

where $\sigma_{\rm T}$ is the Thomson scattering cross section and $P_e = n_e k_B T_e$ is the electron pressure.

Similarly to the calculation for the spectroscopic-like temperature, for our models in non-equipartition and in fully equipartition, we calculate the $\Delta T_{\rm non\text{-}eq/eq}(x)$ by integrating Equation (34) along the line of sight within the shock radius.

Another useful SZ observable is the integrated Comptonization parameter, Y, which is defined as the integration of the Comptonization parameter in Equation (34) on the sky

$$Y = d_A^2 \int y d\Omega = \int y dA, \tag{35}$$

[3] http://cxc.harvard.edu/caldb/prop_plan/imaging/index.html

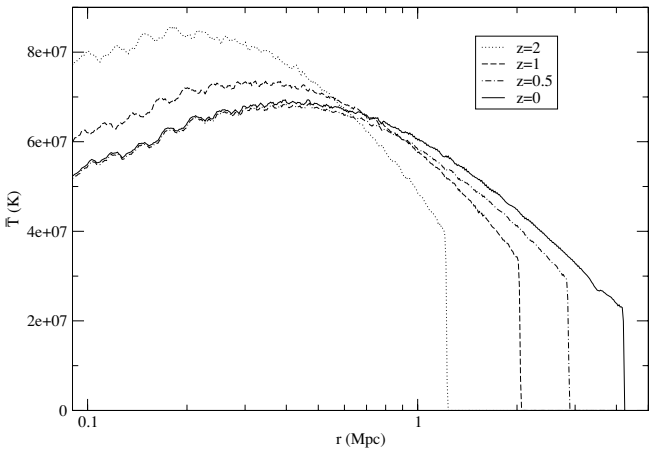

Figure 6. Average thermodynamic temperature profiles of our simulated realistic NFW dark energy model cluster. The hydrodynamic model is the same as in Figure 5.

where d_A is the angular diameter distance to the cluster, Ω is the solid angle of the cluster on the sky, and A is the projected surface area. We integrate the projected surface area of the cluster up to the shock radius. Such a quantity is useful for spatially unresolved clusters with SZ observations where the solid angle covers the whole cluster.

Since $Y = \int y dA \propto \int P_e dV \propto \int n_e T_e dV$, where V is the volume of the cluster, the integrated Comptonization parameter Y is basically measuring the thermal energy of the electrons in the cluster. If electrons and ions are not in equipartition and if the electron temperature is lower than that of the ions globally, the value of Y measured would be lower than the equipartition value. To characterize the degree of non-equipartition of the whole cluster, we define the bias as the ratio $Y_{\rm non\text{-}eq}/Y_{\rm eq}$, where $Y_{\rm non\text{-}eq}$ is the integrated Comptonization parameter for the non-equilibration model and $Y_{\rm eq}$ is that for the equipartition model ($T_e = \bar{T}$).

It has been shown that the integrated Comptonization parameter displays a tight correlation with cluster mass (Reid & Spergel 2006). Such a tight correction is needed for precision cosmology, and hence a correct understanding of the integrated Comptonization parameter is important. A detailed discussion of the use of SZ surveys to study cosmology can be found in Carlstrom et al. (2002).

6.3. Results for the Temperature Profiles and the X-ray Observables

The evolution of the average thermodynamic temperature as a function of radius for a cluster with an accreted mass of $M_{\rm sh} = 1.53 \times 10^{15}\, M_\odot$ at $z = 0$ in the ΛCDM cosmology is shown in Figure 6. In general, for each redshift, the temperature profile rises from the very central region to a peak, and then drops toward the outer region. The drop of temperature in the outer region is due to the drop of the shock velocity during the accretion history. The central drops in temperature, as well as the decrease of the value of the peak temperature are due to the adiabatic expansion of the cluster during the evolution. This is in contrast to the average thermodynamic temperature of the self-similar solution in the Einstein–de Sitter universe where the temperature profile is always rising toward the central region at all redshift (Figure 7), and the temperature within the same gas mass, $M_{\rm gas}$, never drops during the accretion history. The expansion of the hot gas in the central region

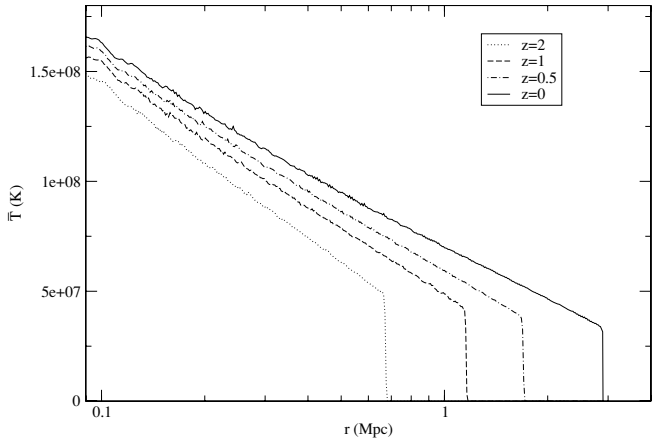

Figure 7. Average thermodynamic temperature profiles of our simulated self-similar dark matter dominated cluster. The hydrodynamic model is the same as in Figure 1.

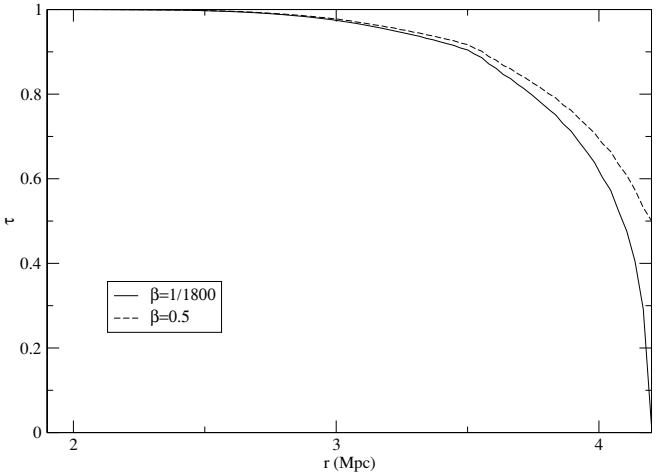

Figure 8. Ratio of electron and average thermodynamic temperatures, $\tau \equiv T_e/\bar{T}$, as a function of radius at $z = 0$. The hydrodynamic model is the same as in Figure 5. The models with shock heating efficiency $\beta = 1/1800$ and 0.5 are shown in solid and dashed lines, respectively.

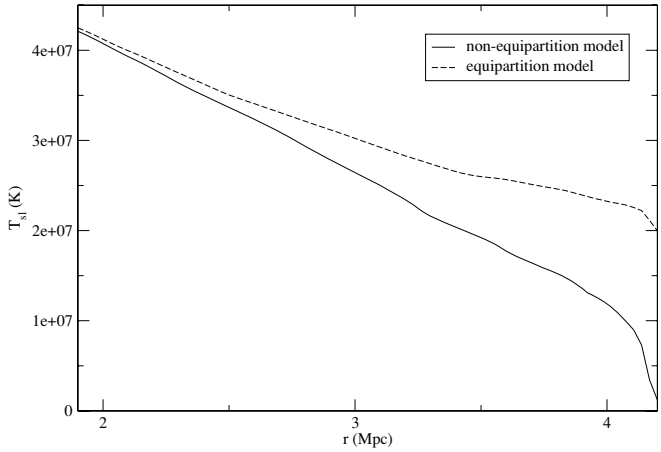

Figure 9. Projected X-ray spectroscopic-like temperature profiles for cluster models at $z = 0$. The hydrodynamic model is the same as in Figure 5. The non-equipartition model with $\beta = 1/1800$ is shown in solid line, while the equipartition model is shown in dashed line. We assume $Z = 0.3\,Z_\odot$ here.

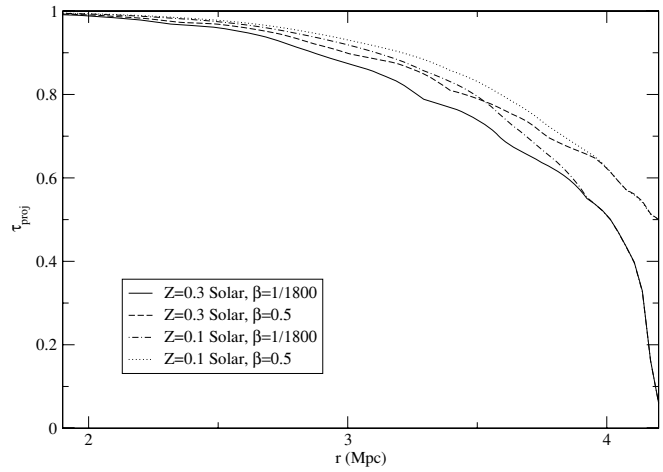

Figure 10. Ratio of the projected X-ray spectroscopic-like temperature profiles of the non-equipartition (with $\beta = 1/1800$ and 0.5) and the equipartition models at $z = 0$. Models with $Z = 0.1$ and $0.3\,Z_\odot$ are presented. The hydrodynamic model is the same as in Figure 5.

of the cluster in our simulation is probably caused by the evolution of the NFW profile, since there is a central pressure drop for the gas in the NFW potential but not for the case in the self-similar model (Section 5). In a real cluster, the temperature profile of the central region ($\lesssim$100 kpc) is likely to be complicated by physical processes such as cooling, AGN heating (Fabian et al. 2000; Blanton et al. 2001), and perhaps thermal conduction (Narayan & Medvedev 2001; Chandran & Maron 2004; Lazarian 2006). On another hand, in the outer region of a cluster, the thermodynamic state is likely to be dominated by gravitational processes and shock heating. Our models have included the essential physics in the outer regions.

Figure 8 shows the ratio of electron and average thermodynamic temperatures, $\tau \equiv T_e/\bar{T}$, as a function of radius for the same cluster at $z = 0$. The shock radius, $R_{\rm sh} \approx 4.2$ Mpc, is about 1.5 times the virial radius, $R_{\rm vir} \approx 2.8$ Mpc. Within the virial radius, the temperature differences between electrons and ions are less than 1%, while beyond $R_{\rm vir}$, $T_e/\bar{T}$ decreases from $\sim$1 to $1/1800$ at the shock radius for the model with $\beta = 1/1800$. For the $\beta = 0.5$ model, $T_e/\bar{T}$ decreases from $\sim$1 to 0.5 at the shock radius. In general, $T_e/\bar{T}$ decreases from $\sim$1 to β at the shock radius for our models. Our models predict that $T_e/\bar{T} \sim 0.8$ at $r \approx 0.9R_{\rm sh} \approx 3.8$ Mpc for a range of β between $1/1800$ and 0.5. Beyond that radius, $T_e/\bar{T}$ depends rather strongly on β. The strong dependence at the shock radius can be used to distinguish shock heating models or constraint the shock heating efficiency of electrons at the shock.

The solid line in Figure 9 shows the projected spectroscopic-like temperature profiles, $T_{\rm sl,non\text{-}eq}$, of the $M_{\rm sh} = 1.53 \times 10^{15}\,M_\odot$ cluster near the outer region at $z = 0$ for our non-equipartition model. We assume $\beta = 1/1800$ and $Z = 0.3\,Z_\odot$ in this figure. For comparison, we also plot the projected spectroscopic-like temperature for a model where equipartition of electrons and ions throughout the cluster is assumed ($T_e = T_i = \bar{T}$) as a dashed line. Both projected temperatures drop in the outer region as the radius increases, but the electron temperature in the non-equipartition model drops faster in most regions shown. Note that for the equipartition model, the projected temperature drop at the very last data point is a numerical artifact instead of a real feature. This is due to the finite resolution of the shock handling in the hydro code which causes a slightly lower temperature compared to the idealized solution. Such an artifact does not affect our results significantly.

The ratio of the projected temperature profiles of the two models, $\tau_{\rm proj} \equiv T_{\rm sl,non\text{-}eq}/T_{\rm sl,eq}$, is plotted in Figure 10. Models

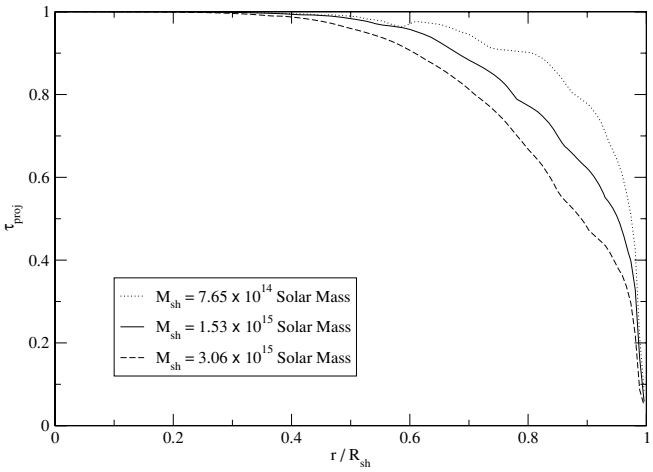

Figure 11. Ratio of the projected X-ray spectroscopic-like temperature of the non-equipartition with $\beta = 1/1800$ and the equipartition models as a function of $r/R_{\rm sh}$ at $z = 0$ for different cluster masses. The hydrodynamic models are similar to those in Figure 5, but with $M_{\rm sh} = 7.65$, 15.3, and $30.6 \times 10^{14}\,M_\odot$ at $z = 0$. We assume $Z = 0.3\,Z_\odot$ here.

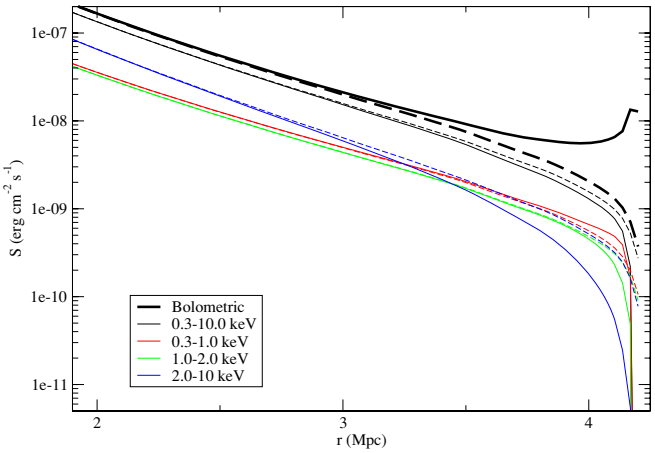

Figure 12. Surface brightness profiles for various energy bands for the non-equipartition (solid lines; thick lines in the print version of the journal) and equipartition (dashed lines; thin lines in the print version) cluster models at $z = 0$. Models are the same as in Figure 9.

(A color version of this figure is available in the online journal.)

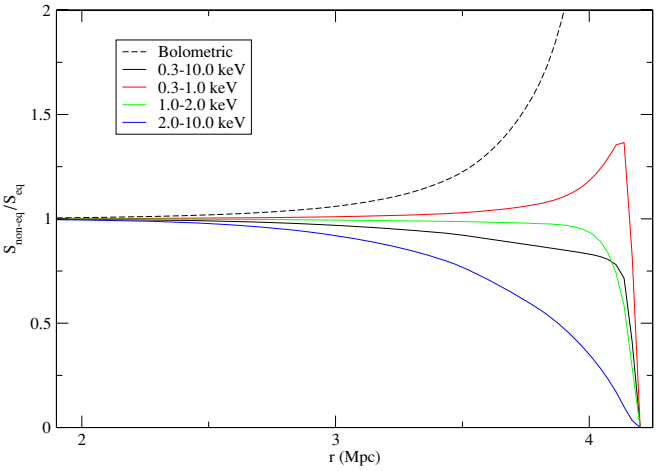

Figure 13. Ratios $S_{\rm non\text{-}eq}/S_{\rm eq}$ as a function of radius. Models are the same as in Figure 12. The ratio of the bolometric surface brightness near the shock radius reaches ∼35 (outside the scale of the figure).

(A color version of this figure is available in the online journal.)

for $\beta = 0.5$ and $Z = 0.1\,Z_\odot$ are also plotted for comparison. Compared to the deprojected (or physical) temperature ratio (Figure 8), the deviation is larger for the projected temperature profiles, which is directly determined observationally. This is because for the projected temperature profile, electrons in the outer region also contribute to the inner region. For models with $\beta = 1/1800$ and $Z = 0.3\,Z_\odot$, there is a ∼10% difference in the projected temperatures for the equipartition and the non-equipartition models at the virial radius ($R_{\rm vir} \approx 2.8$ Mpc) in contrast to less than a percent for the deprojected temperatures. The projected temperature difference increases to about 20% at a radius of ∼3.3 Mpc, which is about 1.2 of the virial radius. Even for $\beta = 0.5$, the difference at this radius can be as large as ∼15%. We also found that the non-equipartition effect on the projected temperature profiles is enhanced by metallicity. From $Z = 0.1$ to $0.3\,Z_\odot$, the deviation at a radius of ∼2.8(3.3) Mpc is enhanced by a factor of ∼1.7(1.5) for the $\beta = 1/1800$ model. This is because the domination of the line emissions in the soft band spectra is enhanced by increasing metallicity, which is more important for the non-equipartition model where electron temperature is lower.

The effect of non-equipartition is larger for more massive clusters. This is shown in Figure 11, where $\tau_{\rm proj}$ for clusters with different masses are plotted versus $r/R_{\rm sh}$. This is because the deviation of the physical temperatures T_e and $\bar{T}$ increases with cluster mass. The behavior qualitatively agrees with the analytic self-similar solution in the Einstein–de Sitter universe found by Fox & Loeb (1997).

The surface brightness profiles for various energy bands of the $M_{\rm sh} = 1.53 \times 10^{15} M_\odot$ cluster near the outer region at $z = 0$ are shown in Figure 12. The ratios $S_{\rm non\text{-}eq}/S_{\rm eq}$ are plotted in Figure 13. We assume $\beta = 1/1800$ and $Z = 0.3\,Z_\odot$ in these figures. For X-ray emission below ∼2 keV, the relative difference between the non-equipartition and the equipartition models is smaller than that of the projected temperature profile. This is because the surface brightness depends on density squared but has a weaker dependence on temperature. The relative difference for X-ray emission above ∼2 keV is similar to that of the projected temperature profile because of the energy cut off for lower temperature. The differences in surface brightness in all energy bands shown are $\lesssim$10% for radii $\lesssim$3 Mpc. Beyond ∼3 Mpc where the electron temperature drops significantly below ∼3 keV for the non-equipartition model, the differences in surface brightness profiles become important. The difference in X-ray surface brightness is most significant for the hard band (2.0–10.0 keV) compared to the soft (0.3–1.0 keV) and medium (1.0–2.0 keV) bands. For the soft band, the surface brightness for the non-equipartition model actually becomes larger than that of the equipartition model at large radii. This is because of the increase in the soft band emissivity for temperature below ∼1 keV. We have also plotted the full X-ray band (0.3–10.0 keV) and the bolometric surface brightness profiles in Figure 12. The full X-ray band surface brightness profile for the non-equipartition model is always lower than that of the equipartition model, while the opposite is true for the bolometric surface brightness profile. This indicates that for the non-equipartition model, a large amount of emission occurs in the energy band below 0.3 keV compared to that of the equipartition model. In fact, the bolometric surface brightness near the shock radius for the non-equipartition model can reach ∼35 times that of the equipartition model.

Current X-ray observations by *Suzaku* of cluster outer regions extend to only $R_{200} \sim 2$ Mpc where the non-equipartition

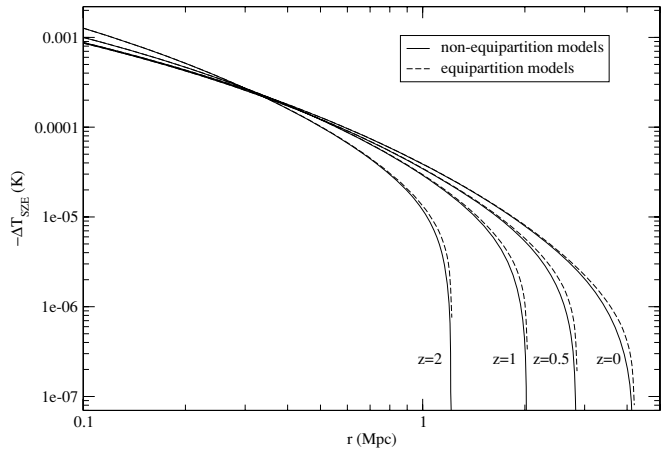

Figure 14. SZ temperature decrement profiles, $-\Delta T_{\rm SZE}$, of our simulated cluster at four different redshifts. The non-equipartition models ($\beta = 1/1800$) are shown in solid lines, while the equipartition models are shown in dashed lines. The hydrodynamic model is the same as in Figure 5.

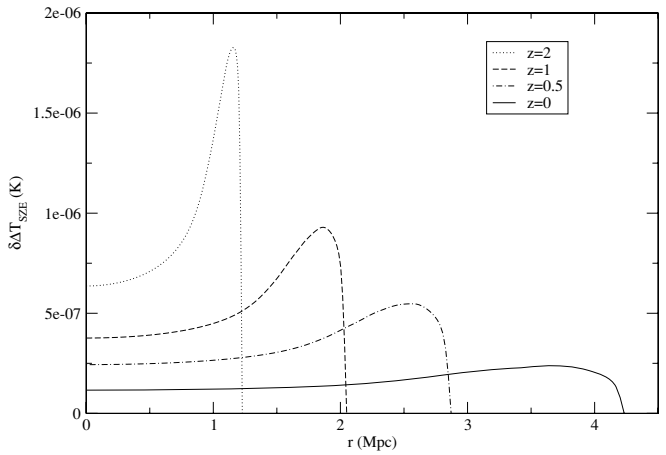

Figure 15. Difference $\delta\Delta T_{\rm SZE}$ between the SZ temperature decrements of the equipartition and the non-equipartition models ($\beta = 1/1800$) at four different redshifts. Models are the same as in Figure 14.

effects on both the surface brightness and projected temperature profiles are $\lesssim$1% in our models. The sensitivities of these observations are limited by the Poisson variations in the background extragalactic source density rather than by the instrumental background (Bautz et al. 2009). To push the sensitivity limit out to $\sim R_{\rm vir} \approx 1.4R_{200}$ where non-equipartition effects on the projected temperature are ∼10%, observations combining high spatial resolution and high surface brightness sensitivity would be needed. On the other hand, increasing the coverage of solid angle can also help to reduce the Poisson variations. Here, we estimate how much improvement in sensitivity would be needed to push the current limit of $\sim R_{200}$ out to $R_{\rm vir} \approx 1.4R_{200}$. Assume most of the current observations only have sensitivities out to R_{200} (but see George et al. 2009) and cluster surface brightness scales as shown in Figure 12. From Figure 12, $S(R_{200}) \sim 6S(1.4R_{200})$ for the 0.3–10.0 keV band, and hence to have a significant detection of X-ray emission at $R_{\rm vir} \approx 1.4R_{200}$, a factor of ∼6 improvement in sensitivity would be needed. Probably a combination of the above two solutions (a factor of 6 improvement in each case) is needed to push the sensitivity limit to $\sim 1.4R_{200}$. Pushing the limit to $R_{\rm sh}$ will be very challenging with X-ray observations. Recently, George et al. (2009) reported that cluster emission has been detected out to $\sim 1.5R_{200}$ in the cluster PKS0745-191. They have shown that the temperature at that radius is ∼30% lower than the temperature predicted by hydrodynamic simulations. If their results are confirmed, we suggest that this may be a signature of electron–ion non-equipartition.

6.4. Results for the SZ Temperature Decrement

Compared to X-ray observations, it is believed that cluster outer regions should be better studied by future SZ observations because the SZ effect depends only on the electron density to the first power, while X-ray emission depends on the electron density squared. The X-ray signature drops much faster compared to the SZ signature. Moreover, the SZ effect is independent of redshift, and a large number of high-redshift clusters should be observable. It has been suggested that future SZ observations such as the Atacama Large Millimeter Array (ALMA) should be able to detect or rule out the presence of accretion shocks in clusters (Kocsis et al. 2005; Molnar et al. 2009).

Figure 14 shows the evolution of the temperature decrement magnitude due to the SZ effect, $-\Delta T_{\rm SZE}$, as a function of radius for a cluster with mass accreted to $M_{\rm sh} = 1.53 \times 10^{15} M_\odot$ at $z = 0$. The solid line shows the non-equipartition model and the dotted line shows the equipartition model. Both the equipartition and non-equipartition models show very similar SZ temperature decrement profiles, with the SZ temperature decrement dropping faster in the non-equipartition models. For the cluster at $z = 0$, $-\Delta T_{\rm SZE}$ drops from ∼1 mK at about 0.1 Mpc down to ∼1 μK at about 3.5 Mpc, and then drops very rapidly beyond that. For the same cluster at $z = 2$ when it had a mass of $M_{\rm sh}(z = 2) = 6.72 \times 10^{14} M_\odot$ (corresponding to $M_{\rm vir} = M_{169} = 5.30 \times 10^{14}\ M_\odot$ at that redshift), the sharp drop in $-\Delta T_{\rm SZE}$ occurs from a higher value of about 10 μK near the shock radius. This suggests that the shock feature can be best studied through high-redshift clusters provided that the region of interest can be spatially resolved. To show the signature of non-equipartition effect more clearly, we plot the difference between the SZ temperature decrements for the equipartition and the non-equipartition models, $\delta\Delta T_{\rm SZE} = \Delta T_{\rm SZE,non\text{-}eq} - \Delta T_{\rm SZE,eq}$, in Figure 15. It shows that the difference is larger at higher redshift for a given cluster. At $z = 2$, $\delta\Delta T_{\rm SZE}$ is of the order of 1 μK for the $M_{\rm sh}(z = 2) = 6.72 \times 10^{14}\ M_\odot$ cluster we considered. The ratios of the temperature decrements (or equivalently the Comptonization parameters), $y_{\rm non\text{-}eq}/y_{\rm eq} = \Delta T_{\rm SZE,non\text{-}eq}/\Delta T_{\rm SZE,eq}$, are also plotted in Figure 16. Similarly to the temperature profiles, for $z = 0$ at the virial radius of $R_{\rm vir} \approx 2.8$ Mpc, $y_{\rm non\text{-}eq}/y_{\rm eq}$ is about 0.93, while it drops to about 0.8 at a radius of ∼3.5 Mpc.

The detailed analysis of whether the effect can be distinguished observationally involves a discussion of the detail characteristic of the potential radio observations, which will be given in an upcoming paper. Here, we only estimate roughly the possibility of whether the non-equipartition signature can be detected at the shock region. We closely follow the estimation done by Kocsis et al. (2005) and Molnar et al. (2009). In their work, they studied whether two different models with and without a shock can be distinguished in future ALMA observations from the SZ effect. In principle, we can adopt their technique directly to distinguish our two models with clusters in equipartition or not. In Figure 10(c) of Molnar et al. (2009), they have argued that for two cluster models with $\delta\Delta T_{\rm SZE}$ of the order of a few μK, the signal-to-noise ratio (S/N) for

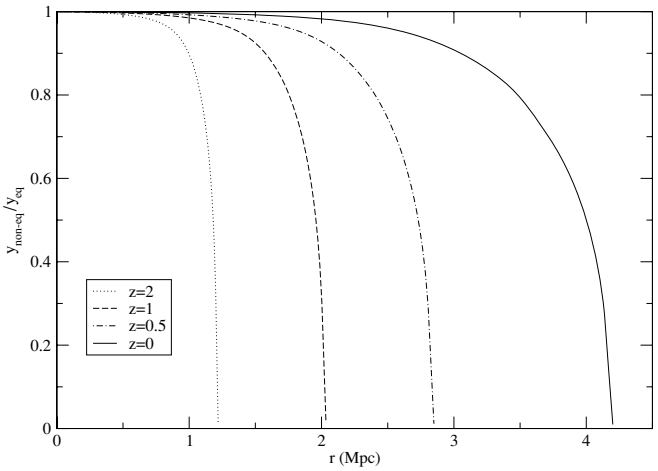

Figure 16. Ratio $y_{\rm non\text{-}eq}/y_{\rm eq}$ between the Comptonization parameters of the equipartition and the non-equipartition models ($\beta = 1/1800$) at four different redshifts. Models are the same as in Figure 14.

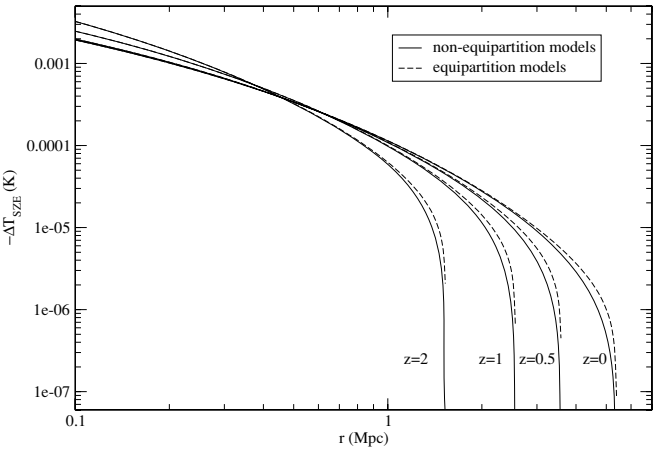

Figure 17. Same as Figure 14 but with $M_{\rm sh}(z = 0) = 3.06 \times 10^{15}\ M_\odot$ for the cluster model.

distinguishing between their models can be as high as 70. For our model with the $M_{\rm sh}(z = 0) = 1.53 \times 10^{15}\ M_\odot$ cluster, $\delta\Delta T_{\rm SZE}$ is less than $\sim 2\ \mu$K even at $z = 2$. However, the most massive cluster today can reach a mass as high as $M_{200}(z = 0) \approx 2 \times 10^{15}\ M_\odot$. In Figure 17, we show the $-\Delta T_{\rm SZE}$ profiles for the equipartition and the non-equipartition models of a cluster with $M_{200}(z = 0) = 1.83 \times 10^{15}\ M_\odot$, which corresponds to $M_{\rm sh}(z = 0) = 3.06 \times 10^{15}\ M_\odot$. The profiles are similar to those of the $M_{\rm sh}(z = 0) = 1.53 \times 10^{15}\ M_\odot$ cluster, except the magnitudes are larger. The shock radius at $z = 2$ is about 1.5 Mpc, which corresponds to an angular size of 177″ for the ΛCDM cosmology we assumed. The mass within the shock radius at $z = 2$ is equal to $M_{\rm sh}(z = 2) = 1.34 \times 10^{15}\ M_\odot$. Figure 18 shows the deviation in $\Delta T_{\rm SZE}$ between the equipartition and non-equipartition models. At $z = 2$, the deviation is $\delta\Delta T_{\rm SZE} \approx 4$–$5\ \mu$K near the shock radius. Closely following Kocsis et al. (2005) and Molnar et al. (2009), we estimate the S/N for distinguishing between the equipartition and the non-equipartition models of the very massive cluster at $z = 2$ by ALMA. Kocsis et al. (2005) estimated that a ∼20 hr on-source integration time for ALMA would be enough to achieve a sensitivity of $\lesssim 10\ \mu$K, but the latest ALMA Sensitivity Calculator[4]

[4] http://www.eso.org/sci/facilities/alma/observing/tools/etc/index.html

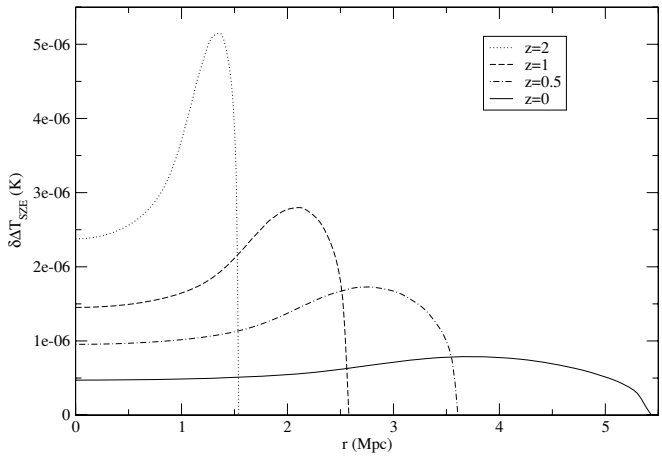

Figure 18. Same as Figure 15 but with $M_{\rm sh}(z = 0) = 3.06 \times 10^{15}\ M_\odot$ for the cluster model.

shows that about 260 hr would be needed for the required angular resolution (FWHM) of 2″ at 100 GHz with 64 antennas. Though such a very long observation is possible, we lower the required angular resolution (FWHM) to 4″ to increase the sensitivity, and the required on-source integration time is reduced to ∼17 hr. Hence we assume a ∼17 hr on-source integration time and estimate the S/N to be $\approx N_{\rm pix}^{1/2}({\rm S/N})_1$, where $N_{\rm pix}$ is the number of independent pixels in the region of interest, and $({\rm S/N})_1$ is the S/N for a single pixel in ALMA. From Figure 18, the width of the annular region of interest from ∼1 to ∼1.5 Mpc is about 0.5 Mpc ∼ 59″ at $z = 2$, where 1 Mpc corresponds to 118″ at this redshift for the standard ΛCDM universe assumed. Assuming a Gaussian beam with an angular diameter (FWHM) of 4″ for ALMA, the number of beams within the region of interest are about $N_{\rm pix} \approx 3000$. In a real cluster, the accretion would likely not to be spherical, and material would accrete through filaments. However, in regions other than the filaments, accretion shocks are roughly spherical and those are the regions which our model may be applied. Molnar et al. (2009) have estimated the area coverage factor of such spherical accretion shock region to be ∼50%. With this correction, $N_{\rm pix,50\%} \approx 1500$. The noise for a single pixel is estimated to be 10 μK (Kocsis et al. 2005; Molnar et al. 2009). We take the signal for a single pixel to be $S_1 \approx \delta\Delta T_{\rm SZE} \approx 4\ \mu$K (Figure 18). Thus, we obtain an S/N of ∼16. Even if the area coverage factor goes down to only 10%, the S/N can still be as high as 7. As noted in Molnar et al. (2009), the sensitivity of interferometers is reduced for large-scale smooth surface density distributions, which is perhaps the case for the SZ effect in the cluster outer regions. The S/N in this analysis may be overestimated. However, they also argue that such a reduction in sensitivity can be recovered by using nonlinear de-convolution of data from mosaic observations (Helfer et al. 2002; Molnar et al. 2009). The above estimation assumes that the cluster model parameters (e.g., cluster mass, shock radius) are known in advance. In real observations trying to distinguish between equipartition and non-equipartition models, if those parameters cannot be obtained by other means, we may need to fit the parameters from the data. This will in general reduce the S/N estimated above. We defer a more detailed study to a future paper, but based on the rather high S/N estimated from the arguments above, we conclude here that future SZ observations, such as those done by ALMA, may be able to distinguish between equipartition and non-equipartition models near the shock region.

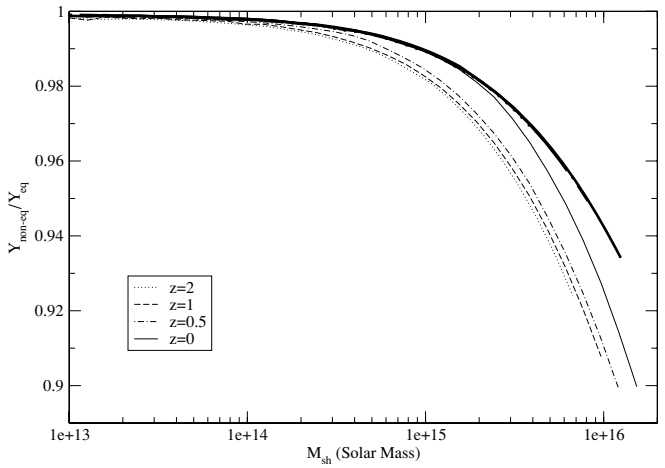

Figure 19. Integrated SZ biases, $Y_{\text{non-eq}}/Y_{\text{eq}}$, as a function of M_{sh} for both our simulated realistic NFW model in the ΛCDM universe (thin lines) and the numerical simulated self-similar model in the Einstein–de Sitter universe (thick lines) at four different redshifts. We assume $f_{\text{gas}} = 0.17$ for models in the Einstein–de Sitter universe. The four lines for the self-similar model lie almost along the same line which cannot be easily distinguished on the graph.

6.5. Results for the Integrated SZ Biases, $Y_{\text{non-eq}}/Y_{\text{eq}}$, and its Evolution

Figure 19 shows the integrated SZ biases, $Y_{\text{non-eq}}/Y_{\text{eq}}$ defined in Section 6.2 as a function of M_{sh} for both our simulated realistic NFW model in the ΛCDM universe and the numerical simulated self-similar model in the Einstein–de Sitter universe at different redshifts. We assume $f_{\text{gas}} = 0.17$ for models in the Einstein–de Sitter universe in Figure 19. The masses are evaluated at the labeled redshift so that the evolutionary history for a particular cluster cannot be seen on the graph. Both models show that $Y_{\text{non-eq}}/Y_{\text{eq}}$ increases as the cluster mass increases, which is expected as the effect of non-equipartition increases with mass. For the realistic NFW model, $Y_{\text{non-eq}}/Y_{\text{eq}}$ decreases from 1 for $M_{\text{sh}} = 10^{13}\,M_{\odot}$ down to ∼0.9 for $M_{\text{sh}} = 10^{16} M_{\odot}$ at $z = 0$. The upper mass limit to which a cluster can grow is limited by the background cosmology as well as the initial density fluctuation amplitudes. The most massive nearby cluster observed has a mass of about $M_{200} \approx 2 \times 10^{15}\,M_{\odot}$, which corresponds to $M_{\text{sh}} \approx 3.3 \times 10^{15}\,M_{\odot}$ in our NFW model. $Y_{\text{non-eq}}/Y_{\text{eq}}$ for the most massive cluster in our universe is hence about 0.97 if it is nearby ($z \approx 0$). This bias would be larger ($Y_{\text{non-eq}}/Y_{\text{eq}}$ smaller in magnitude) at higher redshift for a given mass.

Recent observations suggest that a significant fraction (20%–40%) of the thermal energy is missing from clusters (Ettori 2003; LaRoque et al. 2006; Vikhlinin et al. 2006; Afshordi et al. 2007; Evrard et al. 2008, but see also Giodini et al. 2009). Obviously, if electrons and ions are in non-equipartition, the thermal energy measured by X-ray or SZ observations should be reduced. Our simulations suggest that for cluster with $M_{\text{sh}} \sim 1.5 \times 10^{15}\,M_{\odot}$($M_{200} \sim 10^{15}\,M_{\odot}$), the non-equipartition effect can account for only about 2%–3% of the missing thermal energy. For the most massive clusters, up to 3%–4% of the thermal energy beyond the equipartition value may be stored in the ions near the shock radius, if electrons and ions are in non-equipartition. For M_{sh} smaller than about $5 \times 10^{14} M_{\odot}$ at $z = 0$–2, the non-equipartition effect is less than 1%.

For the self-similar model, the $Y_{\text{non-eq}}/Y_{\text{eq}}$ curves at the four different redshifts actually lie almost along the same line which cannot be easily distinguished from the graph (Figure 19). This shows that the integrated SZ bias for the self-similar model does not evolve with redshift. In contrast, the integrated SZ bias for the realistic NFW model in the ΛCDM universe evolves with redshift. In the ΛCDM universe, the expansion of the universe starts to accelerate around the redshift where $\Omega_M \sim \Omega_\Lambda$; this breaks the self-similar solution for cosmological accretion, and hence we should expect $Y_{\text{non-eq}}/Y_{\text{eq}}$ would also deviate from self-similarity in general. For our realistic NFW model in the ΛCDM universe, the integrated SZ bias decreases as z decreases. This is probably due to the decreasing rate of accretion onto clusters in the ΛCDM universe during the cosmological acceleration, which results in a relatively longer timescale for the electron–ion equilibration inside a cluster compared to a cluster with the same mass in the Einstein–de Sitter universe. At $z = 0$, $Y_{\text{non-eq}}/Y_{\text{eq}}$ of the realistic NFW model is smaller than that of the self-similar model with the same f_{gas} for $M_{\text{sh}} > 10^{15}\,M_{\odot}$, but the effect is similar for $M_{\text{sh}} < 10^{15}\,M_{\odot}$ for both models. At higher redshifts, the effect of non-equipartition is larger for the realistic NFW model for the entire mass range.

Though the magnitude of $Y_{\text{non-eq}}/Y_{\text{eq}}$ is small for the range of cluster masses, even a percentage level deviation in the most massive clusters is important for precision cosmology studies. Cosmological studies using the mass function evolution depend sensitively on the high mass end of clusters. For cluster mass count surveys using Y as a mass proxy, if the bias in Y is not properly taken into account, the resulted mass function would be biased low at the high mass end (i.e., less massive clusters would be observed if clusters are in non-equipartition). Even though the mass–Y relation can be self-calibrated, the evolution of $Y_{\text{non-eq}}/Y_{\text{eq}}$ may introduce a bias if the self-calibration is not properly done at each redshift. For example, if the mass and Y relation is self-calibrated correctly for low-redshift clusters but this calibration is extrapolated to high-redshift clusters, bias would be introduced if the non-equipartition effect is not properly taken into account. A detailed study of the effect of non-equipartition on SZ surveys and the implication to cosmological studies will be presented in an upcoming paper.

7. DISCUSSIONS AND CONCLUSIONS

Using one-dimensional hydrodynamic simulations, we have calculated a sample of realistic NFW clusters in a range of masses in the ΛCDM cosmology. The cluster properties we simulated are consistent with the one-dimensional N-body simulations by Ryu & Kang (1997), and they have shown that their calculations reproduce the density and temperature profiles of the three-dimensional simulated relaxed clusters in the outer regions. Our one-dimensional hydrodynamic simulations help us to isolate the important physical processes under controlled conditions. We have studied in detail the effect of non-equipartition in the outer regions of relaxed clusters in the ΛCDM cosmology.

Using $f_{\text{gas}} = 0.17$ (which is the upper limit for a cluster), we give a conservative lower limit of the non-equipartition effect on clusters. We have shown that for a cluster with a mass of $M_{\text{sh}} \sim 1.5 \times 10^{15}\,M_{\odot}$, within R_{vir}, electron and ion temperatures only differ by less than a percent. Our results show that the effect is smaller than those calculated from recent three-dimensional simulations, which shows that T_e can be biased low by 5% at $R_{200} \sim 0.7 R_{\text{vir}}$ (model CL104 in Rudd & Nagai 2009). A detailed analysis is needed to address the difference, but a possible explanation may be that in a three-dimensional cluster the accretion shock can be formed further in. Our results

show that $T_e/\bar{T}$ can reach ≈0.8 for a range of non-adiabatic electron heating efficiency $\beta \sim 1/1800$ to 0.5 at $\sim 0.9 R_{\rm sh}$ (or $\sim 1.4 R_{\rm vir}$). Beyond that radius, $T_e/\bar{T}$ depends rather strongly on β, and such a strong dependence at the shock radius can be used to distinguish shock heating models or constraint the shock heating efficiency of electron. We also show that the effect of non-equipartition is larger for more massive clusters, which is consistent to analytic self-similar models in the Einstein–de Sitter universe (Fox & Loeb 1997).

Using the algorithm developed by Vikhlinin (2006) which takes into account the soft emission at low temperature down to ∼0.5 keV, arbitrary metallicity, and instrumentation response, we calculated the X-ray spectroscopic-like temperature profiles which are the one to be directly determined observationally. The effect of non-equipartition on the projected temperature profiles is larger than that on the deprojected (or physical) temperature profiles. Non-equipartition effects can introduce a ∼10% bias in the projected temperature at $R_{\rm vir}$ for a wide range of β. This is because for the projected temperature profile, electrons in the outer region also contribute to the inner region. We also found that the effect of non-equipartition on the projected temperature profiles can be enhanced by increasing metallicity. This is because the domination of the line emissions in the soft band spectra is enhanced by increased metallicity, which is more important for the non-equipartition model where the electron temperature is lower.

The effect of non-equipartition on X-ray surface brightness profile in the 0.3–2 keV band is smaller than that on the projected temperature profile. This is because the surface brightness depends on density squared but with a weaker dependence on temperature. This means that in the outer regions, clusters in non-equipartition have similar X-ray surface brightness profile for $E \lesssim 2$ keV, but with bigger difference in temperature compared to those equipartition counterparts. For $E \gtrsim 2$ keV, non-equipartition effects on X-ray surface brightness profiles are similar to those on the projected temperature profiles. For a cluster with $M_{\rm sh} \sim 1.5 \times 10^{15}\, M_\odot$, the effect of non-equipartition on surface brightness profiles in all energy bands is $\lesssim$10% for radii $\lesssim$3 Mpc; beyond that, the effect can be important. We found that for the non-equipartition model, the surface brightness profile in the low-energy band $\lesssim$1 keV can be higher than that of the equipartition model in the cluster outer regions. Non-equilibrium ionization, which was not considered in our calculations of the emissivities, may further enhance the line emissions in the soft bands ($E \lesssim 1$ keV).

Current X-ray observations extend to only $\sim R_{200} \sim 2$ Mpc, although some results from recent *Suzaku* observations begin to go a bit beyond that (George et al. 2009). Within those regions with $\lesssim R_{200}$, electrons and ions should be almost in equipartition and the signatures in the X-ray temperature and surface brightness should be rather weak. But future X-ray observations may extend to $\sim R_{\rm vir} \approx 1.4 R_{200}$ or even close to the shock radius. We have shown that non-equipartition of electrons and ions should be detectable in those studies. The results by George et al. (2009) support our conclusion.

The effects of non-equipartition on the SZ effect were studied. At $z = 0$, the effect on the Comptonization parameters is similar to that of the projected temperature profiles. For a cluster with $M_{\rm sh} \sim 1.5 \times 10^{15}\, M_\odot$, $y_{\rm non\text{-}eq}/y_{\rm eq} \approx 0.93(0.8)$ at $1(1.3) R_{\rm vir}$. For a given cluster, the difference between the SZ temperature decrements for the equipartition and the non-equipartition models is larger at a higher redshift. For the most massive clusters at $z \approx 2$, the differences can be $\delta \Delta T_{\rm SZE} \approx 4$–$5\ \mu$K near the shock radius. A detailed analysis of whether the equipartition and non-equipartition models near the shock region can be distinguished by, for example, ALMA, will be presented in a future paper.

The effects on the integrated SZ Comptonization parameter, which measures the thermal energy content of the electrons, were studied. We have shown that the integrated SZ bias, $Y_{\rm non\text{-}eq}/Y_{\rm eq}$, increases as the cluster mass increases, which is expected as the effect of non-equipartition increases with mass. In general, the non-equipartition effect is larger for the realistic NFW model in the ΛCDM universe than that for the self-similar model in the Einstein–de Sitter universe, assuming that they have the same $f_{\rm gas}$. Our simulations suggest that for relaxed clusters with $M_{\rm sh} \sim 1.5 \times 10^{15}\, M_\odot$, the non-equipartition effect can account for only about 2%–3% of the missing thermal energy globally. For the most massive clusters, up to 4%–5% of the thermal energy beyond the equipartition value may be stored in the thermal energy of ions near the shock radius, but for clusters with $M_{\rm sh} \lesssim 5 \times 10^{14}\, M_\odot$, the non-equipartition effect is less than 1%. Thus, we argue that, at least for relaxed clusters, the non-equipartition effect alone can only account for some of the missing thermal energy problem, if any, for high-mass clusters but not for clusters with smaller masses. On the other hand, this suggests that hot gas may be missing due to other astrophysical processes not yet known, and the $f_{\rm gas}$ in a real cluster should be lower than that we used in our numerical simulations. We have estimated that reducing $f_{\rm gas}$ by 20% will enhance the local non-equipartition effect near the outer region by a few percent, but the integrated SZ bias, $Y_{\rm non\text{-}eq}/Y_{\rm eq}$, is not affected by more than a percent.

We emphasis here that even though non-equipartition effects may not affect the global energy budget significantly, the effect is still important locally in the outer regions ($\sim R_{\rm vir}$) of a cluster. Future X-ray and SZ observations may extend out to $R_{\rm sh}$, and the effect of non-equipartition should be considered when studying cluster properties in those regions.

We found that for our realistic NFW model in the ΛCDM universe, $Y_{\rm non\text{-}eq}/Y_{\rm eq}$ evolves with redshift, which is in contrast to the self-similar model in the Einstein–de Sitter universe. For our realistic NFW model in the ΛCDM universe, $Y_{\rm non\text{-}eq}/Y_{\rm eq}$ decreases as z decreases. This is probably due to the decreasing rate of accretion onto clusters in the ΛCDM universe during the period of cosmological acceleration, which results in a relatively longer timescale for the electron–ion equilibration inside a cluster compared to a cluster with the same mass in the Einstein–de Sitter universe. Though the magnitude of $Y_{\rm non\text{-}eq}/Y_{\rm eq}$ is small for the range of cluster masses, even a percentage level deviation in the most massive clusters can be important for precision cosmology studies. Such a variation of Y with z would introduce an apparent evolution in $f_{\rm gas}$, which would bias the cosmological studies using the $f_{\rm gas}$ techniques (Allen et al. 2008). Recently, Rudd & Nagai (2009) have shown that the non-equipartition effect on Y can be enhanced by major mergers up to 30%, although for low Mach number mergers, the shock heating efficiency for electrons may be higher which can weaken the non-equipartition effect (Ghavamian et al. 2007; Markevitch & Vikhlinin 2007). The temporary boost due to mergers may have a significant effect on the estimation of cosmological parameters using clusters. We defer a detailed study of the effect on cosmology studies in a future paper.

K.W. thanks Avi Loeb and Brian Mason for helpful discussions. Support for this work was provided by the

National Aeronautics and Space Administration, through *Chandra* Award Numbers TM7-8010X, GO7-8135X, GO8-9083X, and GO9-0035X, NASA *XMM-Newton* grants NNX08AZ34G, NNX08AW83G, and NASA *Suzaku* grant NNX08AI27G. We thank the referee for helpful comments.

APPENDIX

EXPRESSION FOR ELECTRON HEATING WITHIN THE SHOCK

Adiabatic changes in electron temperature are given by

$$(T_{e2})_{\rm ad} = \left(\frac{\rho_{e2}}{\rho_{e1}}\right)^{\gamma-1} T_{e1}\,, \tag{A1}$$

where $\rho_{e2}/\rho_{e1} = \rho_{g2}/\rho_{g1}$ for fully ionized plasma. In addition to the adiabatic heating, electrons can also be heated by non-adiabatic processes. From the definition of non-adiabatic electron heating efficiency (Equation (26)), the change of electron temperature due to non-adiabatic heating is

$$(\Delta T_e)_{\rm non\text{-}ad} = \beta(\Delta \bar{T})_{\rm non\text{-}ad}. \tag{A2}$$

Thus, the final electron temperature can be expressed as

$$T_{e2} = \left(\frac{\rho_{g2}}{\rho_{g1}}\right)^{\gamma-1} T_{e1} + (\Delta T_e)_{\rm non\text{-}ad}. \tag{A3}$$

Similarly for the average thermodynamic temperature, we have

$$(\bar{T}_2)_{\rm ad} = \left(\frac{\rho_{g2}}{\rho_{g1}}\right)^{\gamma-1} \bar{T}_1 \tag{A4}$$

and

$$\begin{aligned}\left(\Delta\bar{T}\right)_{\rm non\text{-}ad} &= \bar{T}_2 - \left(\bar{T}_2\right)_{\rm ad} \\ &= \bar{T}_2 - \left(\frac{\rho_{g2}}{\rho_{g1}}\right)^{\gamma-1} \bar{T}_1\,.\end{aligned} \tag{A5}$$

Combining Equations (A2), (A3), and (A5), we get

$$T_{e2} = \left(\frac{\rho_{g2}}{\rho_{g1}}\right)^{\gamma-1} T_{e1} + \beta\ \max\left[0, \bar{T}_2 - \left(\frac{\rho_{g2}}{\rho_{g1}}\right)^{\gamma-1} \bar{T}_1\right], \tag{A6}$$

where a minimum of zero in the second term is set to ensure that numerical fluctuations do not introduce false decreases in entropy in the non-adiabatic heating.

REFERENCES

Afshordi, N., Lin, Y.-T., Nagai, D., & Sanderson, A. J. R. 2007, MNRAS, 378, 293
Allen, S. W., Rapetti, D. A., Schmidt, R. W., Ebeling, H., Morris, R. G., & Fabian, A. C. 2008, MNRAS, 383, 879
Bautz, M. W., et al. 2009, PASJ, in press (arXiv:0906.3515)
Bertschinger, E. 1985, ApJS, 58, 39
Blanton, E. L., Sarazin, C. L., McNamara, B. R., & Wise, M. W. 2001, ApJ, 558, L15
Borgani, S., & Kravtsov, A. 2009, Adv. Sci. Lett., in press (arXiv:0906.4370)
Bryan, G. L., & Norman, M. L. 1998, ApJ, 495, 80
Bullock, J. S., Kolatt, T. S., Sigad, Y., Somerville, R. S., Kravtsov, A. V., Klypin, A. A., Primack, J. R., & Dekel, A. 2001, MNRAS, 321, 559
Buote, D. A., Gastaldello, F., Humphrey, P. J., Zappacosta, L., Bullock, J. S., Brighenti, F., & Mathews, W. G. 2007, ApJ, 664, 123
Bykov, A. M., Dolag, K., & Durret, F. 2008a, Space Sci. Rev., 134, 119
Bykov, A. M., Paerels, F. B. S., & Petrosian, V. 2008b, Space Sci. Rev., 134, 141
Carlstrom, J. E., Holder, G. P., & Reese, E. D. 2002, ARA&A, 40, 643
Chandran, B. D. G., & Maron, J. L. 2004, ApJ, 602, 170
Chieze, J.-P., Alimi, J.-M., & Teyssier, R. 1998, ApJ, 495, 630
Chuzhoy, L., & Loeb, A. 2004, MNRAS, 349, L13
Dolag, K., Bartelmann, M., & Lesch, H. 2002, A&A, 387, 383
Dolag, K., Bartelmann, M., Perrotta, F., Baccigalupi, C., Moscardini, L., Meneghetti, M., & Tormen, G. 2004, A&A, 416, 853
Ettori, S. 2003, MNRAS, 344, L13
Ettori, S., & Fabian, A. C. 1998, MNRAS, 293, L33
Evrard, A. E., et al. 2008, ApJ, 672, 122
Fabian, A. C., et al. 2000, MNRAS, 318, L65
Fox, D. C., & Loeb, A. 1997, ApJ, 491, 459
Gao, L., Navarro, J. F., Cole, S., Frenk, C. S., White, S. D. M., Springel, V., Jenkins, A., & Neto, A. F. 2008, MNRAS, 387, 536
George, M. R., Fabian, A. C., Sanders, J. S., Young, A. J., & Russell, H. R. 2009, MNRAS, 395, 657
Ghavamian, P., Laming, J. M., & Rakowski, C. E. 2007, ApJ, 654, L69
Giodini, S., et al. 2009, ApJ, 703, 982
Helfer, T. T., Vogel, S. N., Lugten, J. B., & Teuben, P. J. 2002, PASP, 114, 350
Hu, W., & Kravtsov, A. V. 2003, ApJ, 584, 702
Hull, A. J., Scudder, J. D., Larson, D. E., & Lin, R. 2001, J. Geophys. Res., 106, 15711
Kaastra, J. S., & Mewe, R. 1993, A&AS, 97, 443
Kang, H., Ryu, D., Cen, R., & Ostriker, J. P. 2007, ApJ, 669, 729
Kocsis, B., Haiman, Z., & Frei, Z. 2005, ApJ, 623, 632
LaRoque, S. J., Bonamente, M., Carlstrom, J. E., Joy, M. K., Nagai, D., Reese, E. D., & Dawson, K. S. 2006, ApJ, 652, 917
Lazarian, A. 2006, ApJ, 645, L25
Li, Y., Mo, H. J., van den Bosch, F. C., & Lin, W. P. 2007, MNRAS, 379, 689
Liedahl, D. A., Osterheld, A. L., & Goldstein, W. H. 1995, ApJ, 438, L115
Loeb, A. 2007, J. Cosmol. Astropart. Phys., JCAP03(2007)001
Makino, N., Sasaki, S., & Suto, Y. 1998, ApJ, 497, 555
Markevitch, M., & Vikhlinin, A. 2007, Phys. Rep., 443, 1
Mazzotta, P., Rasia, E., Moscardini, L., & Tormen, G. 2004, MNRAS, 354, 10
Medvedev, M. V. 2007, ApJ, 662, L11
Mewe, R., Gronenschild, E. H. B. M., & van den Oord, G. H. J. 1985, A&AS, 62, 197
Mignone, A., Bodo, G., Massaglia, S., Matsakos, T., Tesileanu, O., Zanni, C., & Ferrari, A. 2007, ApJS, 170, 228
Molnar, S. M., Hearn, N., Haiman, Z., Bryan, G., Evrard, A. E., & Lake, G. 2009, ApJ, 696, 1640
Narayan, R., & Medvedev, M. V. 2001, ApJ, 562, L129
Navarro, J. F., Frenk, C. S., & White, S. D. M. 1995, MNRAS, 275, 720
Neto, A. F., et al. 2007, MNRAS, 381, 1450
Rakowski, C. E., Ghavamian, P., & Hughes, J. P. 2003, ApJ, 590, 846
Reid, B. A., & Spergel, D. N. 2006, ApJ, 651, 643
Reiprich, T. H., et al. 2009, A&A, 501, 899
Rudd, D. H., & Nagai, D. 2009, ApJ, 701, L16
Ryu, D., & Kang, H. 1997, MNRAS, 284, 416
Sarazin, C. L. 1986, Rev. Mod. Phys., 58, 1
Schekochihin, A. A., Cowley, S. C., Kulsrud, R. M., Hammett, G. W., & Sharma, P. 2005, ApJ, 629, 139
Schekochihin, A. A., Cowley, S. C., Kulsrud, R. M., Rosin, M. S., & Heinemann, T. 2008, Phys. Rev. Lett., 100, 081301
Spitzer, L. 1962, Physics of Fully Ionized Gases (2nd ed.; New York: Interscience)
Takizawa, M. 1999, ApJ, 520, 514
Tozzi, P., Scharf, C., & Norman, C. 2000, ApJ, 542, 106
Vikhlinin, A. 2006, ApJ, 640, 710
Vikhlinin, A., Kravtsov, A., Forman, W., Jones, C., Markevitch, M., Murray, S. S., & Van Speybroeck, L. 2006, ApJ, 640, 691
Wechsler, R. H., Bullock, J. S., Primack, J. R., Kravtsov, A. V., & Dekel, A. 2002, ApJ, 568, 52
Wong, K.-W., Sarazin, C. L., Loeb, A., & Wik, D. R. 2008, in The Warm & Hot Universe, ed. F. Paerels (Greenbelt, MD: NASA/GSFC), http://warmhot.gsfc.nasa.gov/Posters/Poster07_Wong.pdf
Zhao, D. H., Jing, Y. P., Mo, H. J., & Börner, G. 2003a, ApJ, 597, L9
Zhao, D. H., Jing, Y. P., Mo, H. J., & Börner, G. 2009, ApJ, 707, 354
Zhao, D. H., Mo, H. J., Jing, Y. P., & Börner, G. 2003b, MNRAS, 339, 12